NAVAL POSTGRADUATE SCHOOL

MONTEREY, CALIFORNIA

THESIS

HIGH-ENERGY ELECTRON IRRADIATION OF HIGH-EFFICIENCY THIN-FILM GALLIUM ARSENIDE SOLAR CELLS

by

Matthew G. Murdock

June 2018

Thesis Advisor: Sherif N. Michael
Second Reader: Matthew A. Porter

Approved for public release. Distribution is unlimited.

REPORT DOCUMENTATION PAGE	*Form Approved OMB No. 0704-0188*

1. AGENCY USE ONLY ***(Leave blank)***	**2. REPORT DATE** June 2018	**3. REPORT TYPE AND DATES COVERED** Master's thesis

4. TITLE AND SUBTITLE HIGH-ENERGY ELECTRON IRRADIATION OF HIGH-EFFICIENCY THIN-FILM GALLIUM ARSENIDE SOLAR CELLS	**5. FUNDING NUMBERS**
6. AUTHOR(S) Matthew G. Murdock	
7. PERFORMING ORGANIZATION NAME(S) AND ADDRESS(ES) Naval Postgraduate School Monterey, CA 93943-5000	**8. PERFORMING ORGANIZATION REPORT NUMBER**
9. SPONSORING / MONITORING AGENCY NAME(S) AND ADDRESS(ES) N/A	**10. SPONSORING / MONITORING AGENCY REPORT NUMBER**

11. SUPPLEMENTARY NOTES The views expressed in this thesis are those of the author and do not reflect the official policy or position of the Department of Defense or the U.S. Government.

12a. DISTRIBUTION / AVAILABILITY STATEMENT Approved for public release. Distribution is unlimited.	**12b. DISTRIBUTION CODE** A

13. ABSTRACT (maximum 200 words)

The electrical power supplied to satellites will continue to be provided by solar cells for the foreseeable future and new technologies and better methods of production for these cells will continue to be developed. Additionally, the space environment within the Earth's radiation belts and the effect of the radiation on solar cells within this environment is well documented. The effects of radiation on solar cells outside this environment with the use of an 8-MeV electron beam was investigated. Thin-film high-efficiency gallium arsenide test devices were characterized, and an analysis of the thin-film devices' performance post-irradiation was conducted via illuminated DC current-voltage and external quantum efficiency measurements. The results of this analysis showed a drastic reduction in device short circuit current of over 95% by a total electron fluence of 10^{16} cm^{-2}.

14. SUBJECT TERMS thin-film, solar cells, electron irradiation, GaAs, high-energy, space	**15. NUMBER OF PAGES** 93
	16. PRICE CODE

17. SECURITY CLASSIFICATION OF REPORT Unclassified	**18. SECURITY CLASSIFICATION OF THIS PAGE** Unclassified	**19. SECURITY CLASSIFICATION OF ABSTRACT** Unclassified	**20. LIMITATION OF ABSTRACT** UU

NSN 7540-01-280-5500

Standard Form 298 (Rev. 2-89)
Prescribed by ANSI Std. 239-18

THIS PAGE INTENTIONALLY LEFT BLANK

HIGH-ENERGY ELECTRON IRRADIATION OF HIGH-EFFICIENCY THIN-FILM GALLIUM ARSENIDE SOLAR CELLS

Matthew G. Murdock
Lieutenant, United States Navy
BS, Boise State University, 2009

Submitted in partial fulfillment of the
requirements for the degree of

MASTER OF SCIENCE IN ELECTRICAL ENGINEERING

from the

NAVAL POSTGRADUATE SCHOOL
June 2018

Approved by: Sherif N. Michael
Advisor

Matthew A. Porter
Second Reader

R. Clark Robertson
Chair, Department of Electrical and Computer Engineering

THIS PAGE INTENTIONALLY LEFT BLANK

ABSTRACT

The electrical power supplied to satellites will continue to be provided by solar cells for the foreseeable future, and new technologies and better methods of production for these cells will continue to be developed. Additionally, the space environment within the Earth’s radiation belts and the effect of the radiation on solar cells within this environment is well documented. The effects of radiation on solar cells outside this environment with the use of an 8-MeV electron beam was investigated. Thin-film high-efficiency gallium arsenide test devices were characterized, and an analysis of the thin-film devices’ performance post-irradiation was conducted via illuminated DC current-voltage and external quantum efficiency measurements. The results of this analysis showed a drastic reduction in device short circuit current of over 95% by a total electron fluence of 10^{16} cm^{-2}.

THIS PAGE INTENTIONALLY LEFT BLANK

TABLE OF CONTENTS

LIST OF FIGURES

THIS PAGE INTENTIONALLY LEFT BLANK

LIST OF TABLES

THIS PAGE INTENTIONALLY LEFT BLANK

ACKNOWLEDGMENTS

I would like to thank Professor Sherif Michael and Mr. Matthew Porter for their guidance, expertise and other assistance in the completion of this thesis. Without their help, this research would not have been possible. Additionally, I would like to give my appreciation to the team at the Idaho Accelerator Center for their expertise and professionalism during the radiation tests. Finally, I could not have performed the tasks required for this thesis research without the steady purpose my wife provides. Thank you to everyone involved.

THIS PAGE INTENTIONALLY LEFT BLANK

I. INTRODUCTION

The development of the solar cell began in the 19th century with the groundbreaking discovery of the photovoltaic effect. This was observed when the first photovoltaic cell was developed in 1839 by the French physicist Edmond Becquerel [1]. The advancement of solar cell technology during the following 170+ years has been dramatic, allowing the use of sunlight as a source of electrical power for many applications. These applications can be separated into two categories, terrestrial and space. For the purpose of this thesis, the space application is the focus.

From the dawn of the space age until now the importance of orbiting satellites is undeniable. They are used by commercial and defense entities alike for many purposes ranging from global communication and navigation to surveillance and missile defense. With the current technology, satellites are launched with all of the systems and hardware already onboard, and the lifetime of the satellite is limited by the lifetime of this hardware. Non-renewable energy sources are not used due to their energy-to-weight ratio. Utilizing the sun as a renewable power source is the most desirable solution to this problem.

The use of solar cells in space is not without its own complications. The performance of semiconductor devices degrades significantly when exposed to radiation. The main sources of radiation of interest for orbiting satellites are from protons and electrons trapped in the Van Allen belts, heavy ions trapped in the magnetosphere, cosmic ray protons and heavy ions, and protons and heavy ions from solar flares [2].

Since 1976, the National Renewable Energy Laboratory (NREL) has reported solar-cell conversion efficiency records for all different types of solar cells. The types of solar cells that perform with the highest conversion efficiency are multi-junction cells. For reference, the highest efficiency ever recorded without the use of a solar concentrator is 38.8% by a five-junction cell from Spectrolab in 2013 [3]. The state-of-the-art solar cells used for space applications today, however, are not as efficient. Typical space cells used are the Spectrolab NeXt triple-junction (XTJ) cells, with a maximum power efficiency of 29.5% [4]. Thin film technology has improved drastically over the past decade, and efficiencies have risen from 5% to 10% in the 1970s to over 28% in 2012 [3]. Further investigation into the suitability for thin films in space should be performed.

A. PREVIOUS WORK AT NPS

Previous work involving high-energy electron irradiation of solar cells at NPS is limited. In 1986, Gold realized the need to investigate the performance of gallium arsenide (GaAs) solar cells after high-energy electron irradiation to determine damage coefficients for open-circuit voltage V_{oc}, short-circuit current I_{sc}, and maximum power output [5]. Gold utilized the NPS linear accelerator (LINAC) to produce electrons at 20.0 MeV and found the maximum power output for these cells decreased by 50% after a total electron fluence of 10^{15} cm^{-2} [5]. Fifer attempted to utilize the NPS LINAC to examine the damage mechanism of a commercially available multi-junction solar cell when irradiated by a 90-MeV electron beam in 2001 [6]; however, he was only able to obtain a single data point due to an equipment failure in the LINAC [6]. Finally, in 2002, Woods made a performance comparison between Si, GaAs, and a triple-junction solar cell post-irradiation using the NPS LINAC [7]. Woods performed the radiation tests at an electron energy of 30.0 MeV and up to a total fluence of 10^{16} cm^{-2} [7]. The results of the 30-MeV tests indicated the GaAs and triple-junction cells showed little to no reduction in performance characteristics until a total fluence of greater than 10^{14} cm^{-2}, while the Si cell had a nearly linear reduction in performance over the entire range of fluence and was determined to be the least suitable for operation in a radiation environment [7].

B. THESIS OBJECTIVE

The objective of this thesis is to evaluate the performance of high-efficiency thin-film GaAs solar cells before and after irradiation by high-energy electrons. The standard energy used in most solar cell radiation effects research is 1.0 MeV. In this thesis, we investigate the effect of higher energy electrons, specifically 8.0 MeV, on the solar cells. The devices under test are commercially available GaAs thin-film cells manufactured by Alta Devices [3]. Solar cell performance is characterized before and after radiation testing via standard illuminated DC current–voltage measurement. In addition, a system to perform external quantum efficiency (EQE) is developed and used to measure the radiation effects upon the spectral response of the cells. The solar cells were exposed to electron irradiation by an 8.0-MeV electron beam generated by a LINAC at Idaho State University (ISU). The test devices were characterized immediately after irradiation via current-voltage measurement. The devices were subjected to varying radiation doses up to a total fluence of 10^{16} cm^{-2}, and the same characterization was repeated. The EQE measurements were performed at varying radiation doses upon return to Monterey.

In this thesis, we begin with a review of semiconductor physics and solar cells fundamentals in Chapter II. A discussion of radiation and its effects on semiconductors, specifically photovoltaic cells, is provided in Chapter III. The experimental methods and test set-ups are discussed in Chapter IV. The procedure and results from the radiation tests is given in Chapter V. Finally, the conclusion of the thesis is given in Chapter VI.

THIS PAGE INTENTIONALLY LEFT BLANK

II. SOLAR CELL FUNDAMENTALS

In order to understand the operation of a solar cell, some basic semiconductor physics is reviewed. A common material used in solar cells and other semiconductor devices is Si, which is a Group IV material, so called because it has four electrons in its outermost valence shell. These valence electrons are shared to create covalent bonds between atoms, as seen in Figure 1.

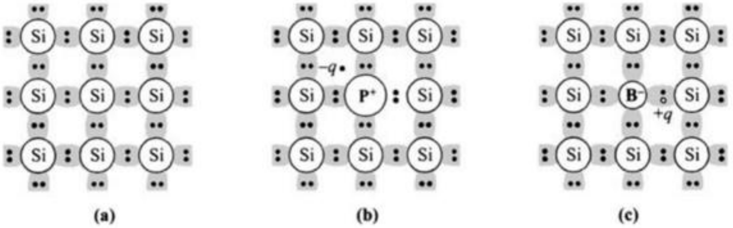

(a) Intrinsic Si with no impurity. (b) n-type Si with donor (phosphorus). (c) p-type Si with acceptor (boron).

Figure 1. Three Basic Bond Pictures of a Semiconductor. Source: [8].

When the atoms of a semiconductor are shared like this, it creates a crystalline structure. At very low temperatures, all of the electrons have low energy and are confined to the valence band of the structure [9]. When enough energy is transferred to a valence electron, such as by the introduction of a photon, the electron can move to the conduction band. The amount of energy required to move an electron from the valence band energy E_v to the conduction band energy E_c for a given material is called the bandgap energy E_g [8]. When an electron moves into the conduction band, it becomes a free carrier available for conduction. The departure of this electron from the valence band creates a vacancy or a hole. This hole can be thought of as a free carrier with a positive charge equal in magnitude to that of an electron.

The band structure of a semiconductor can either be a direct-gap or indirect-gap type. This distinction refers to the location of the minimum conduction band energy. In a direct-gap material it is located at the same wave vector (Γ) as the maximum valence band energy and in an indirect-gap material it is located at a different wave vector. A diagram illustrating the bandgap of a direct-gap and an indirect-gap semiconductor is represented in Figure 2. For the purpose of this thesis, wave vector can be thought of as a momentum in the crystal and is not discussed further.

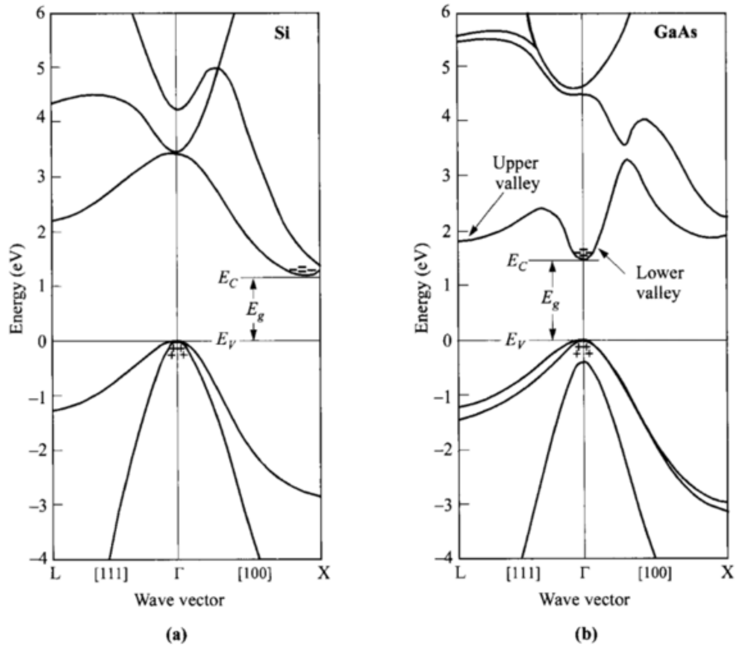

The (+) signs indicate holes in the valence band and the (-) signs indicate electrons in the conduction bands. Indirect-gap material is shown in (a) and direct-gap material is shown in (b).

Figure 2. Energy-Band Structures. Source: [8].

In order to change the existing balance of free carriers, the semiconductor material is deliberately doped with impurity atoms [8]. Dopant atoms that contain more valence electrons than the host material are called *n*-type dopants, or donors, while dopant atoms that contain fewer valence electrons are called *p*-type dopants, or acceptors. In an *n*-type semiconductor the electron concentration *n* is much larger than the hole concentration *p*; therefore, electrons are referred to as the majority carrier in an *n*-type semiconductor and holes are referred to as the minority carrier. The reverse is true for a *p*-type semiconductor. Both cases are displayed in Figure 3.

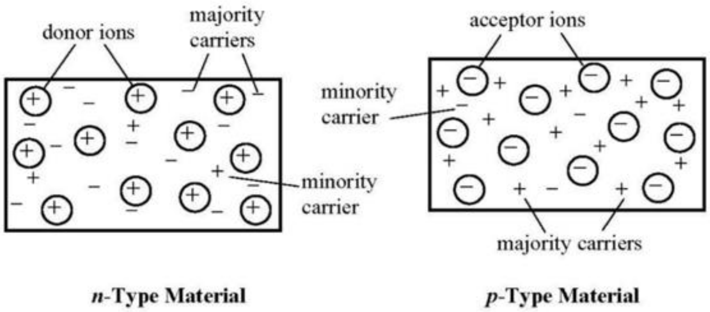

Figure 3. Illustration of *n*-type and *p*-type Semiconductor Materials. Source: [10].

A. OPTICAL CARRIER GENERATION IN SEMICONDUCTORS

Every semiconductor material is characterized by a bandgap energy E_g, required to free an electron from the outermost valence shell of the atom, thus creating an electron-hole pair [11]. This energy can be transferred to the electron via photons. Each photon has energy *hf*, where *h* is Planck’s constant and *f* is the frequency of the light. This energy can be expressed as

$$hf\left(eV\right) = h\frac{c}{\lambda} = \frac{1.24}{\lambda\left(\mu m\right)} \tag{1}$$

where *c* is the speed of light and λ is the wavelength of the light. Any excess photon energy absorbed above E_g is dissipated in the material as heat.

The light absorption coefficient α for a given semiconductor material is a function of photon wavelength or energy and is the inverse of average photon penetration depth [8]. For energies less than E_g, the light absorption coefficient is essentially zero, as shown in Figure 4. The sharp rise in α near E_g for GaAs is representative of direct-gap semiconductors, while the gradual increase for Si is representative of an indirect-gap semiconductor [11]. This property of direct-gap semiconductors can be taken advantage of in devices to absorb nearly all incident photons with less material thickness than that of an indirect-gap material [11].

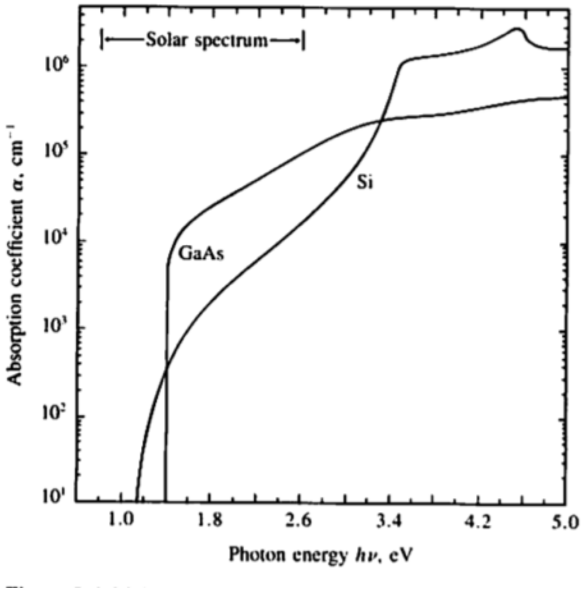

Figure 4. Light Absorption Coefficient as a Function of Photon Energy for Si and GaAs. Source: [11].

Photon transport through semiconductors can be determined by taking into account the photon absorption within the material. The number of photons per square centimeter per second, or photon flux, as a function of distance travelled in a semiconductor is

$$F\left(x\right) = F_o e^{-\alpha x} \tag{2}$$

where x is the distance travelled in the semiconductor, F_o is the photon flux incident on the surface, and α is the light absorption coefficient of the semiconductor [11]. Additionally, the carrier generation rate G given in units of carriers per unit volume is

$$G(x) = \frac{-\,dF(x)}{dx} = \alpha F_o e^{-\alpha x}. \tag{3}$$

B. CARRIER RECOMBINATION PROCESSES

Photo-generated carriers can also be removed from a semiconductor via recombination processes. Recombination occurs when an electron and hole recombine to annihilate each other. The rate at which excess electrons and holes recombine is the recombination rate R given in units of carriers per unit volume. Recombination rate is described an [11] as

$$R = \frac{n - n_o}{t} = \frac{p - p_o}{t} \qquad (4)$$

where n and p are the electron and hole densities, respectively, n_o and p_o are the equilibrium electron and hole densities, respectively, and τ is the carrier lifetime.

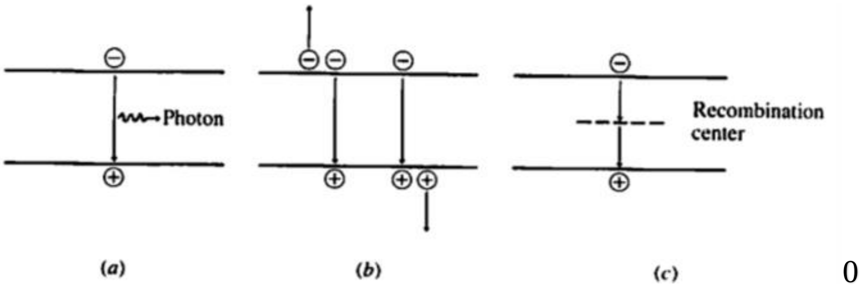

(a) Band-to-band recombination, (b) Auger recombination, and (c) Recombination through recombination centers.

Figure 5. Important Recombination Mechanisms. Source: [11].

This recombination process can take place through several physical processes, illustrated in Figure 5. Band-to-band recombination occurs when an electron transitions from the conduction band to the valence band or can be thought of as a hole transitioning from the valence band to the conduction band. This process is the reverse of photon absorption, and during this loss of energy, equal to E_g, a photon is emitted. This process is more probable for direct-gap semiconductors such as GaAs [8]. The Auger process is similar to the band-to-band recombination except when the carrier transitions across the bandgap it transfers its energy in the form of kinetic energy to another carrier [11]. The third major recombination process is by recombination centers or traps [11]. Traps are defects in the material that can introduce intermediate energy levels in the forbidden region between E_c and E_v. These defects may be caused by impurities introduced purposefully or as by-products of the manufacturing process [12]. Additionally, defects can be introduced through radiation damage, and the reduction of carrier lifetime via defect introduction is one of the primary processes through which radiation exposure affects semiconductor devices [9]. In addition to inducing recombination, defects can also act as traps for electrons and holes, removing them from the free carrier population.

All recombination processes can be combined into a total recombination rate as the sum of the three separate rates

$$\frac{1}{\tau}=\frac{1}{\tau_{band-band}}+\frac{1}{\tau_{Auger}}+\frac{1}{\tau_{trap}} \tag{5}$$

where τ is the total recombination lifetime and $\tau_{band\text{-}band}$, τ_{Auger}, and τ_{trap} are the recombination lifetimes for band-to-band, Auger, and trap recombination processes, respectively [11].

C. P-N JUNCTIONS

The structure of a solar cell in its basic form is a *p-n* junction. A *p-n* junction is formed when a *p*-type semiconductor is placed in contact with an *n*-type semiconductor [9]. Due to the difference in the carrier concentrations of these materials, electrons tend to diffuse to the *p*-type side of the junction and recombine with the majority holes [10]. Conversely, holes tend to diffuse to the *n*-type material and recombine with the majority electrons [10]. A region forms that is mostly depleted of carriers where only a layer of positive ions and a layer of negative ions remain [10]. This space containing the two charge layers is called the depletion region, or the space-charge region [11]. The charge in the depletion region creates an electric field that opposes further movement of the diffused electrons and holes [10]. An illustration of a *p-n* junction is shown in Figure 6.

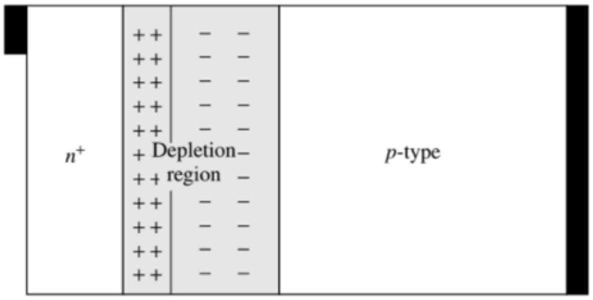

Figure 6. Illustration of *p-n* Junction. Source: [13].

D. SOLAR RADIATION

A solar cell converts optical energy into electrical energy. The most important source of optical energy on Earth is our sun. A nuclear fusion reaction occurs in the sun where approximately 6.0×10^{11} kg of hydrogen is converted to helium per second [8]. During this reaction there is a net mass loss between the hydrogen and helium of about 4.0×10^3 kg, which is converted to 4.0×10^{20} J of energy and is emitted primarily as electromagnetic radiation [8]. As the light from sun penetrates the Earth's atmosphere, some of the light is attenuated. The attenuation is primarily from water-vapor absorption in the infrared region, ozone absorption in the ultraviolet region, and overall scattering due to airborne dust and aerosols [8]. The magnitude in which the atmosphere affects the intensity of sunlight is called the air mass (AM) number. The AM number is defined as the secant of the angle between the sun and the zenith [8]. The integrated intensity of solar radiation corresponding to different AM numbers is shown in Table 1.

Table 1. Solar Power Densities Corresponding to Different Air Mass Values. Adapted from [10].

Air Mass Number	**Solar Power Density (W/m^2)**
AM0	1367
AM1	1086
AM1.5	982
Overcast	104

The intensity of the solar spectrum outside the Earth's atmosphere is represented by AM0, or zero air mass. This is the only air mass of importance for satellites in an Earth orbit and closely resembles black body radiation at approximately 5,800 K [8]. The power spectral density for different AM numbers as well as a 5,800 K black body is shown in Figure 7.

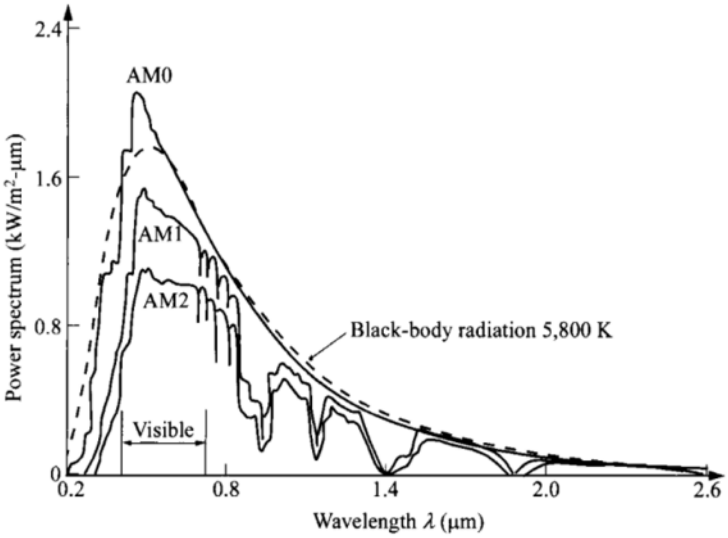

Figure 7. Solar Spectrum at Various Air Mass Values. Source: [8].

E. SOLAR CELL PARAMETERS

As mentioned previously, a solar cell is essentially a *p-n* junction with a load connected to output contacts on either side of the depletion region, as shown in Figure 8.

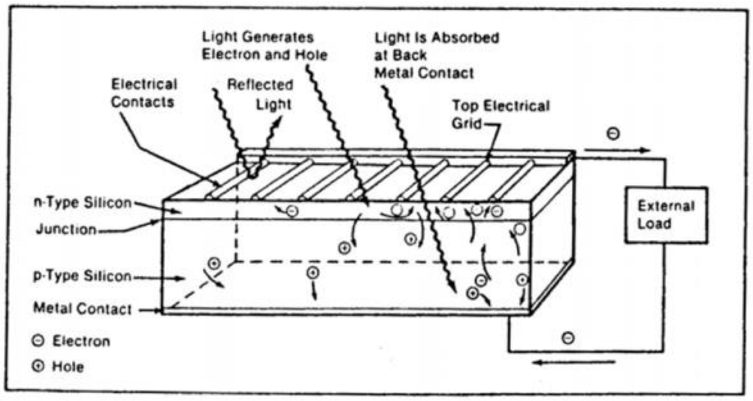

Figure 8. Illustration of a Silicon Solar Cell with Connected Load Under Illumination. Source: [10].

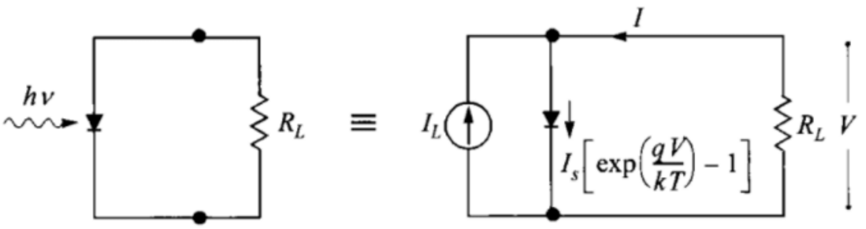

Figure 9. Ideal Equivalent Solar Cell Circuit Under Illumination. Source: [8].

When a solar cell is exposed to sunlight, there are many different photon energies present. A photon with energy less than E_g does not contribute to overall device output current as it cannot produce an electron-hole pair. In an ideal solar cell circuit, the photocurrent is determined by assuming every photon of sufficient energy produces one electron-hole pair. An idealized solar cell circuit is shown in Figure 9, where I_L is the photocurrent, I_s is the diode saturation current, and R_L is the load resistance. The current through the solar cell without illumination is called the dark current I_{dark} and is approximated by

$$I_{dark} \approx I_s\left[\exp\left(\frac{qV}{kT}\right) - 1\right] \tag{6}$$

where q is the elementary charge, V is the voltage across the cell, k is Boltzmann's constant, and T is the absolute temperature in K [8]. The total I-V characteristics of an ideal device under illumination is a summation of the dark current and the photocurrent given by [8] as

$$I = I_s\left[\exp\left(\frac{qV}{kT}\right) - 1\right] - I_L . \tag{7}$$

A plot of typical I-V characteristics of a solar cell under illumination is shown in Figure 10.

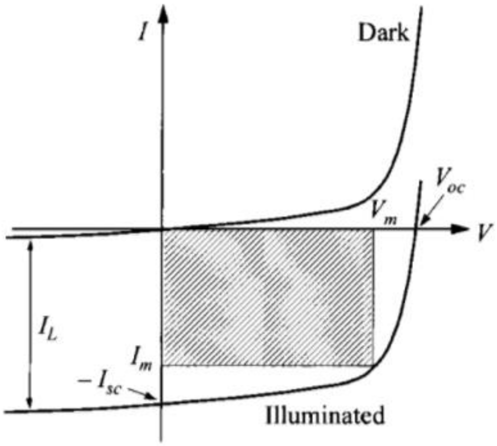

Figure 10. I-V Characteristics of a Solar Cell Under Illumination. Source: [8].

Several parameters that characterize the performance of a solar cell are discussed in the following paragraphs. The short-circuit current I_{sc} of a cell is I_L when the output terminals are shorted together, or V is equal to zero. The open-circuit voltage V_{oc} is the voltage that develops across an illuminated cell under open circuit conditions. The output power P_{out} of a solar cell is the product of cell current and voltage given by

$$P_{out} = IV = I_s V\left[\exp\left(\frac{qV}{kT}\right) - 1\right] - I_L V . \tag{8}$$

The maximum power operating point is the point (I_m,V_m) on the I-V characteristics plot at which the cell operates with the greatest possible conversion efficiency. From the product of I_m and V_m the maximum power can be determined as

$$P_m = I_m V_m = F_F I_{sc} V_{oc} \approx I_L\left[V_{oc} - \frac{1}{b}\ln(1+bV_m) - \frac{1}{b}\right] \tag{9}$$

where

$$b = \frac{q}{kT} . \tag{10}$$

Another useful property when characterizing solar cells is called the fill factor F_F, which is a metric of resistive loss within the solar cell. The fill factor is defined as

$$F_F = \frac{I_m V_m}{I_{sc} V_{oc}} . \tag{11}$$

Finally, the ideal power conversion efficiency is the ratio of the maximum power output to the incident solar power, given by

$$\eta = \frac{P_m}{P_{in}} = \frac{I_m V_m}{P_{in}} = \frac{F_F I_{sc} V_{oc}}{P_{in}} \tag{12}$$

where P_{in} is the incident solar power on the cell. In order to increase conversion efficiency, it is clearly desirable to increase I_{sc}, V_{oc}, and F_F as shown by Equation 12.

1. Factors that Affect Efficiency

Other factors that can affect conversion efficiency are bandgap energy, cell temperature, recombination lifetime, doping density, light blockage, reflection from metal contacts, and light intensity [11].

Bandgap energy affects conversion efficiency with competing mechanisms. An increase in E_g increases a cell's V_{oc}; however, it decreases the maximum possible I_{sc} due to the decreased amount of absorption of the solar spectrum, which peaks between 1.0 and 2.0 eV [11]. This leads to a conversion efficiency peak for a certain E_g as shown in Figure 11.

The parameters of the *p*-*n* junction are crucial to good solar cell performance. Doping density can have a substantial impact on a cell's V_{oc}. For light to moderate doping there is an increasing trend in V_{oc} with increasing doping density; however, a heavy-doping effect reduces V_{oc} when base doping exceeds 10^{18} cm^{-3} for silicon solar cells as displayed in Figure 12 [14]. This reduction in V_{oc} is referred to as bandgap narrowing, and heavy doping in GaAs shows similar effects [15].

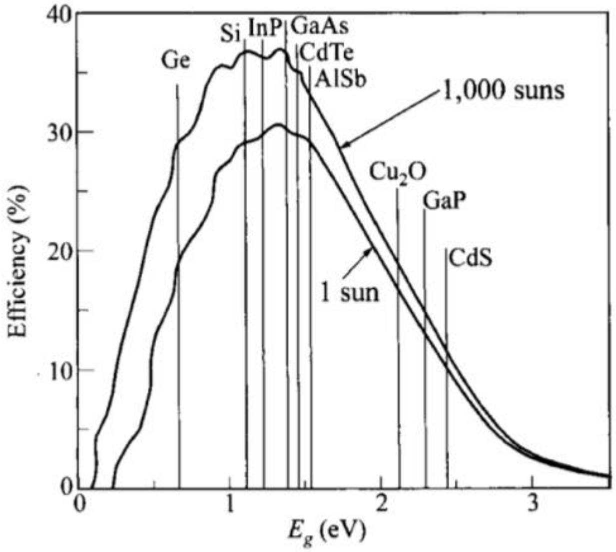

Shown under AM 1.5 conditions at 300 K
for one sun and 1,000-sun concentration.

Figure 11. Ideal Solar Cell Conversion Efficiency as a Function of E_g. Source: [8].

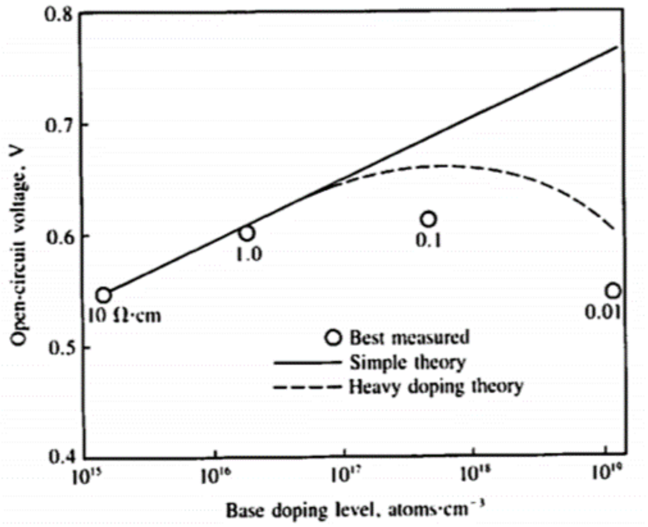

Figure 12. Open-Circuit Voltage as a Function of Base Doping Density for a Silicon Solar Cell. Source: [14].

Increasing carrier-recombination lifetime τ helps achieve a larger I_{sc} and reduces dark current, thereby increasing V_{oc} [11]. Indirect-gap materials require much larger recombination lifetimes to achieve the same efficiency as direct-gap materials [8]. This is another reason direct-gap materials are more desirable for solar cells. As previously discussed, recombination lifetime is reduced with the introduction of more traps which may be caused by manufacturing impurities, or more importantly for this thesis, radiation damage. Finally, as temperature of the cell is increased, the V_{oc} varies according to

$$\frac{dV_{oc}}{dT} = \frac{1}{q}\frac{dE_g}{dT} - \frac{1}{T}\left(\frac{E_g}{q} - V_{oc}\right) \tag{13}$$

where T is temperature in K [11]. A GaAs solar cell operating at 333 K shows an open-circuit voltage temperature dependence dV_{oc}/dT of approximately 2 mV/K [16]. For example, a 10-K increase in temperature reduces the cell's V_{oc} by about 0.02 V, decreasing the overall power efficiency of the cell.

2. Spectral Response

Another measure of a solar cell's efficiency at converting optical energy into electrical energy is called spectral response (SR). The SR is the ratio of the number of collected carriers to the number of photons entering the cell [11]. This ratio is also called external quantum efficiency (EQE) and is referred to as such for the remainder of this thesis. It is called EQE because it is a function of the photons incident on the surface of the solar cell or external to the device. The EQE is given by

$$EQE = \frac{electrons/\mathrm{s}}{photons/\mathrm{s}} = \frac{I_{ph}(\lambda)}{qAf(\lambda)} \tag{14}$$

where $I_{ph}(\lambda)$ is the photocurrent as a function of photon wavelength, A is the solar cell surface area, and $f(\lambda)$ is the photon flux incident on the solar cell as a function of photon wavelength [13]. The EQE of an Alta Devices cell is shown in Figure 14.

The change in EQE qualitatively shows the degradation of the devices versus material thickness or depth [8]. It has been shown that photons of different energies interact in different regions of a solar cell as illustrated in Figure 13 [8]. The generation rate $G(\lambda,x)$ is shown to occur at a shallower depth in the device with photons of higher energies and at greater depth for photons of lower energies [8]. The EQE results can, therefore, be used to indicate the depth of majority damage by electron irradiation by observing the change in magnitude at different photon wavelengths.

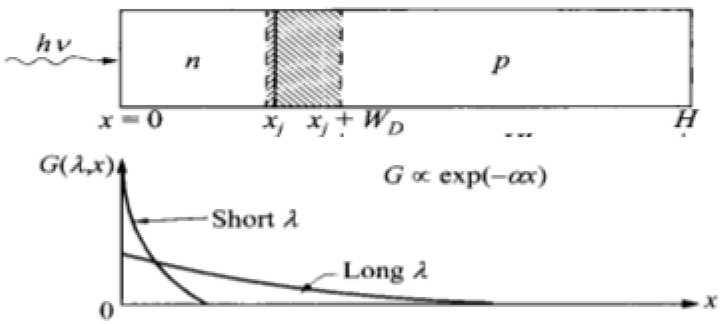

Figure 13. Generation Rate as a Function of Solar Cell Thickness. Adapted from [8].

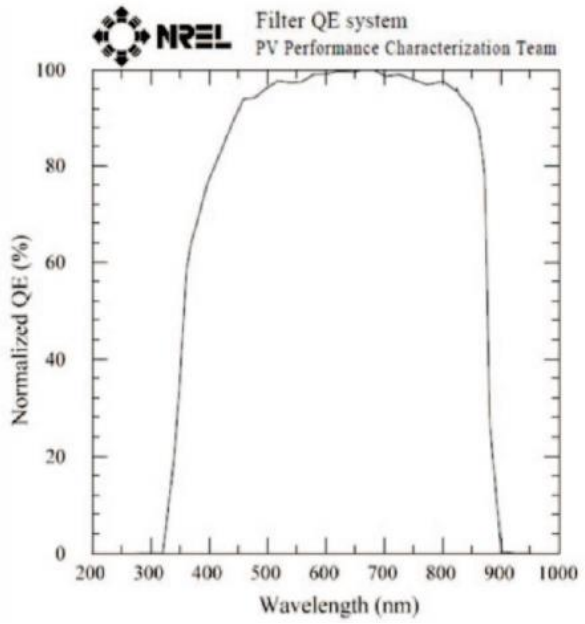

Figure 14. EQE of Alta Devices’ GaAs Thin-Film Solar Cell Certified by NREL. Source: [17].

F. ADVANCED THIN-FILM SOLAR CELLS

As the demand for higher efficiency and lower cost solar cells continues, new technologies and processes will be discovered. Although thin-film technology is not new, the conversion efficiency of thin-film solar cells has risen greatly in the past decade. When thin-film solar cells were first produced in the 1970s, the efficiency was only 5% to 9% for cells fabricated from $CuIn_xGa_{1-x}Se_2$ (CIGS) and CdTe [3]. Current solar cells utilized in space are thin film by necessity, achieved by wafer thinning processes, and can achieve efficiencies of around 30% using a multi-junction structure [18].

The method in which thin-film GaAs cells are grown is called metalorganic chemical vapor deposition (MOVCD) [19]. This process begins with a GaAs crystal wafer which acts as growth medium for additional layers to be deposited; this is called epitaxial growth. The crystal wafers are then heated to 800° C, and a crystal layer of aluminum arsenide (AlAs) is deposited on the surface with tremethylaluminum and arsine gases. Next, crystalline layers of GaAs are grown on the AlAs with trimethylgallium and arsine gases. Metal contacts are then deposited on the existing structure. Finally, the AlAs layer is chemically etched away with hydrofluoric acid, and a thin-film solar cell remains. This final process is called epitaxial lift-off (ELO). The GaAs crystal wafer is then cleaned and reused [19]. GaAs solar cells have been available for over 40 years but are expensive to manufacture due to wafer costs. The ELO process allows for wafer re-use and lower-cost devices. High-efficiency thin-film GaAs cells were first developed and tested by Radboud University in the Netherlands [20]. These cells were verified by the National Renewable Energy Laboratory (NREL) in 2005 with an efficiency of about 23% [3]. In 2012, Alta Devices developed a thin-film GaAs cell that currently holds the world record for efficiency of a single-junction cell at 28.8% [3]. This rise in conversion efficiency for thin-film GaAs has led to the examination of their use in future space applications.

As mentioned previously, GaAs is a direct-gap semiconductor and only requires a very thin active layer of several microns, where an indirect-gap semiconductor, such as Si, requires approximately 100 microns to absorb all incident photons [17]. In addition, the band-to-band recombination in GaAs can emit another photon for use in photo-generation of carriers, called photon recycling [17]. Photon recycling and the high light absorption coefficient of GaAs for the majority of the solar spectrum allows thin-film GaAs solar cells to have such a high conversion efficiency.

Thin-film GaAs solar cells now boast conversion efficiencies that rival those of current space solar cells. There are several advantages that thin-film cells can provide over current multi-junction space cells, such as structural flexibility and lower mass for the same output power. Thin-film GaAs cells are also promising for space applications due to an intrinsic radiation hardness as a function of film thickness. Recent research at Arizona State University examined the radiation response of varying thicknesses of GaAs thin-film single-junction cells under 1.0-MeV electron exposure [20]. Solar cell EQE measurements before and after irradiation and relative efficiency loss at different radiation doses are shown in Figure 15, demonstrating increased performance for the thinner film cell after exposure [20].

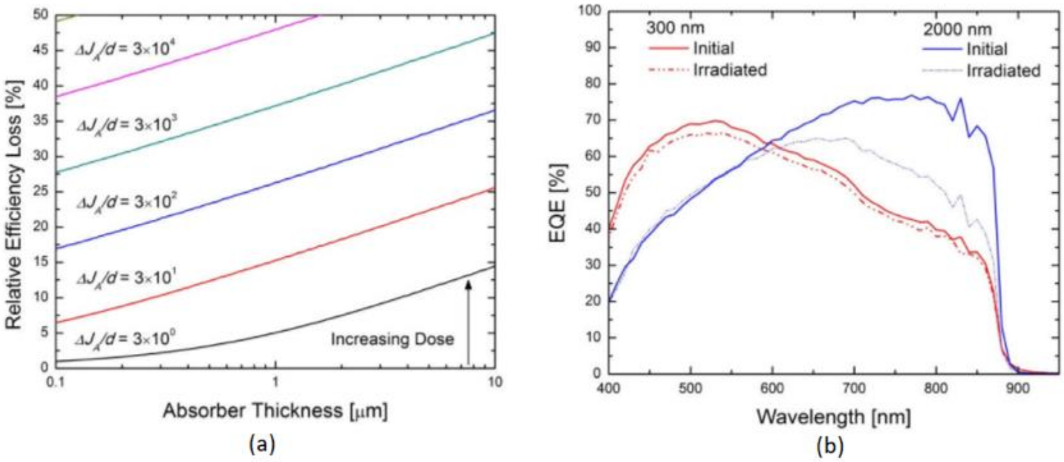

Figure 15. (a) Modeled Relative Efficiency Loss (b) Measured EQE for 300 nm and 2,000 nm. Adapted from [21].

III. RADIATION EFFECTS ON SOLAR CELLS

A. SPACE RADIATION ENVIRONMENT

Operating in space exposes solar cells to a high level of background radiation not encountered in terrestrial applications. This leads to degradation of the cells over time. The primary radiation environment in Earth orbit can be divided into two categories, particles trapped by Earth's magnetic field and transient events [2]. The particles trapped by Earth's magnetic field are called the Van Allen radiation belts [22]. The Van Allen belts are comprised of an inner belt containing mostly electrons and protons and an outer belt consisting of mostly electrons [9]. Transient events of concern to solar cells operating in space are galactic cosmic rays (GCR) and solar flares. GCR are mostly made up of heavy ions and hydrogen. Solar flares can produce highly energetic protons and heavy ions. Particles that can produce permanent damage and associated typical energies are listed in Table 2 [9]. Damaging electromagnetic radiation, such as gamma rays, are of minor importance in the natural space environment for solar cells when compared to particles already mentioned and are not discussed further [9].

Table 2. Particles that Produce Permanent Damage. Adapted from [9].

Particle	**Energy Range (MeV)**	**Source**
Protons	0.1 to 500	Inner Van Allen belt and Solar Flares
Electrons	up to 7	Inner and outer Van Allen belts
GCR	up to 20,000	Deep space

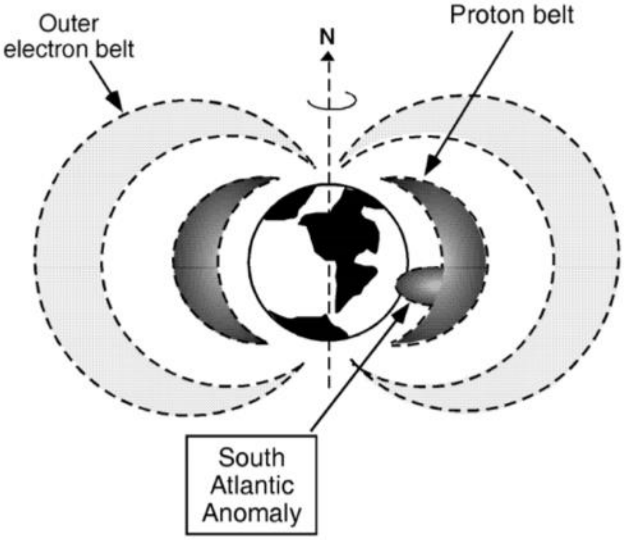

Figure 16. Simple Diagram of Earth’s Trapped Radiation Belts. Source: [9].

The amount of radiation received by a solar cell is largely dependent on orbit altitude and inclination. Unlike the simple diagram of the Van Allen belts shown in Figure 16, the contours of radiation are not constant with altitude above the Earth’s surface and vary with orbital inclination and by the hemisphere which is sun facing [9]. Addtionally, the magnetic field includes a region over the southern hemisphere where the inner radiation belt extends to a much lower altitude called the South Atlantic Anomaly (SAA) [9].

Four Earth orbits are shown in Figure 17. The orbit with the lowest altitude is the low Earth orbit (LEO). LEO contains any orbit in the range of 160 to 2000 km altitude [23]. This orbit is generally considered the least damaging in regards to radiation exposure. The Earth’s magnetic field provides a region of low radiation; however, satellites can still be heavily influenced by the SAA where the inner Van Allen belt altitude is reduced to approximately 200 km [9].

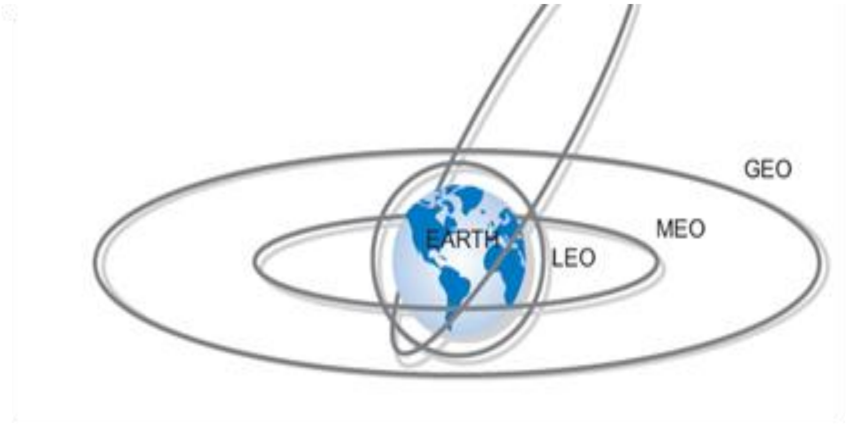

Figure 17. Typical Earth Orbits. Source: [23].

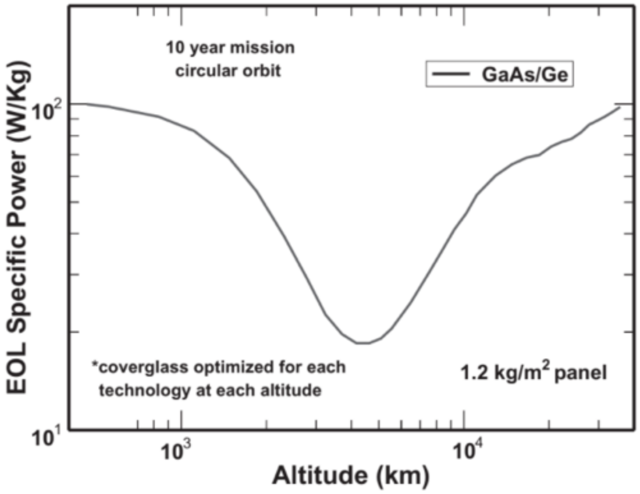

Figure 18. End-of-Life Specific Power for Single-Junction GaAs Cell as Function of Altitude. Source: [22].

The next orbit is the medium Earth orbit (MEO). MEO extends from the range of 2,000 to 20,350 km [23]. This is the worst orbit for solar cells to operate in due to the presence of energetic protons that extend from approximately 6,400 to 24,000 km altitude [9]. The effect of operation at this orbit can be seen in Figure 18, where the largest reduction in end-of-life (EOL) specific power can be seen around an altitude of 4,000 to 5,000 km [22]. Next, the geosynchronous Earth orbit (GEO) is at the altitude of 35,786 km, where the satellite orbits at the same speed the Earth is rotating about its axis [23]. This orbit is within the outer radiation belt where electrons are the dominant source of damaging radiation [9]. Finally, the highly elliptical orbit (HEO) has an altitude that can range from 500 km at perigee to 40,000 km at apogee [23]. Satellites in this orbit traverse both inner and outer Van Allen belts. Outside of GEO and HEO, such as for deep space travel, the dominant sources of damaging radiation are solar flares and GCR [9].

Other planets in our solar system have magnetic fields that trap radiation similar to the Van Allen radiation belts. The strongest planetary magnetic field in our solar system belongs to Jupiter with a magnetic moment about 20,000 times greater than that of Earth [24]. A model of the electron flux plotted as function of electron energy for different Jupiter orbits is shown in Figure 19, where R_J is the radius of Jupiter and is 71,492 km [25]. It is evident that a significant portion of the electrons surrounding Jupiter have an energy greater than or equal to 10 MeV.

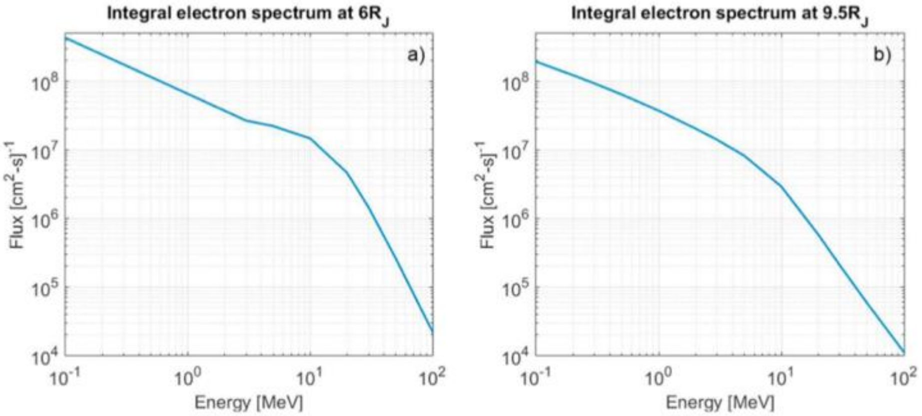

Figure 19. Model of Jupiter Electron Spectrum for a) 6 R_J and b) 9.5 R_J. Source: [24].

In addition to static background radiation fields, transient events such as solar flares can introduce higher energy electrons of 3.0 to 12.0 MeV to spacecraft outside Earth’s magnetosphere [26]. These events are of concern for space missions that involve interplanetary travel.

B. RADIATION DAMAGE MECHANISMS IN SEMICONDUCTORS

There are several different physical processes in which radiation interacts with materials. The two primary damage mechanisms of concern to semiconductor materials are ionization and displacement damage [9].

1. Ionization

Ionization occurs when an incoming charged particle removes an electron bound to an atom of the semiconductor. The electron is moved from the valence band to the conduction band, and an electron-hole-pair is created in a similar fashion to a photon produced electron-hole-pair. The typical minimum energy required for a charged particle produced electron-hole-pair is between 2.2 and 4.0 times the bandgap energy, for GaAs 4.7 eV [9]. Ionization usually takes place in insulating regions such as oxides used in solar cells and results in the creation of charge traps near interface regions [9]. Additionally, the transmittance of cover glass can be reduced, reducing the amount of light incident on the solar cell [13].

2. Displacement Damage

Displacement damage occurs when an incoming particle transfers enough energy to an atom in the material to move it out of its original lattice position, creating a vacancy [9]. The target atom must absorb a minimum energy for displacement, called the displacement threshold energy, which is closely related to the atomic binding energy of the material [9]. When the amount of energy transferred is around the same magnitude as the displacement threshold energy, a vacancy-interstitial pair is formed as shown in Figure 20, called a Frenkel pair [9].

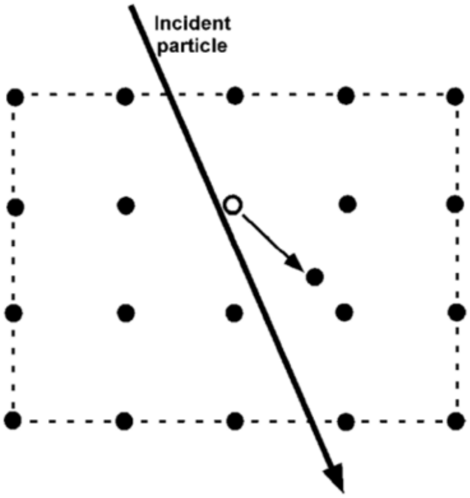

Figure 20. Displacement of a Lattice Atom Forming a Frenkel Pair. Source: [9].

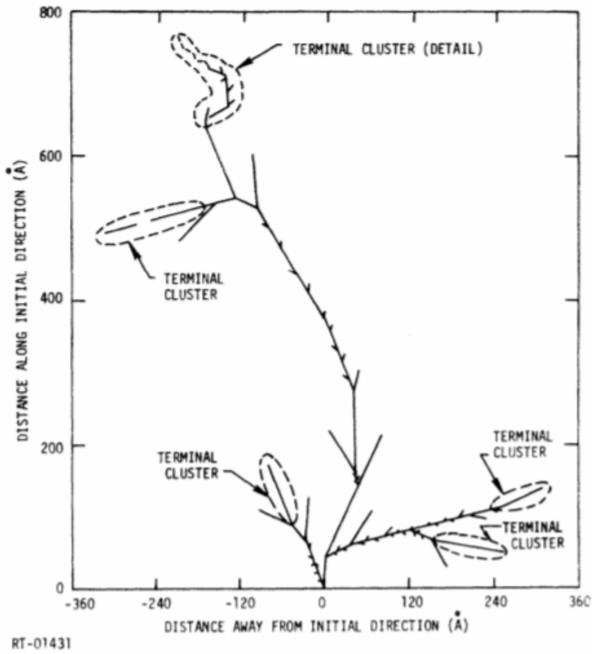

Figure 21. Simulation of Displacement Damage in Silicon for 50 keV Recoil Atom. Source: [27].

When the energy transferred by the incoming particle is much larger than the threshold energy, the initial atom involved in the collision can have sufficient energy to create further displacements in the lattice [9]. This initial atom is referred to as the primary knock-on atom (PKA) or recoil atom [9]. In the case of a much higher energy transfer (≥

1keV), cascade damage regions can form where there are clusters of vacancies and interstitials in a localized region of the material [9]. The results of a Monte Carlo simulation of displacement damage in silicon where 50 keV was absorbed by the PKA is shown in Figure 21.

C. EFFECTS OF RADIATION DAMAGE ON SEMICONDUCTOR PROPERTIES

When exposed to radiation, ionization of electrons and displacement of lattice atoms affects specific properties of a semiconductor. The properties most influenced are minority carrier lifetime, carrier density, and carrier mobility [9]. The dependence on fluence of these parameters is shown in Figure 22 for 50.0-MeV protons. Minority carrier lifetime is one of the properties that can be greatly affected by displacement damage and is reduced after damage occurs [9]. The change in minority carrier lifetime can be related to fluence by

$$\frac{1}{\tau} - \frac{1}{\tau_o} = \frac{\Phi}{K_{tau}} \tag{15}$$

where τ is the minority carrier lifetime after irradiation, τ_o is the initial minority carrier lifetime, Φ is the particle fluence, and K_{tau} is the lifetime damage constant [9].

Displacement damage introduces additional defects into the material which act as traps for free carriers. The carrier density is affected by this increase in carrier removal by the simple relation

$$\Delta n = R_c \Phi \tag{16}$$

where Δn is the change in carrier density after irradiation and R_c is the carrier removal coefficient [9]. Carrier removal is not only significantly affected by displacement damage but is often the primary source of performance reduction for compound semiconductors such as GaAs [9].

Another property affected by displacement damage is carrier mobility. The addition of defects that act as traps within the semiconductor bandgap also increase the effect of scattering, which reduces the carrier mobility by the basic relation

$$\frac{\mu_o}{\mu} = 1 + \beta\Phi \tag{17}$$

where μ_o is the initial mobility, μ is the mobility after irradiation, and β is the associated damage constant [9].

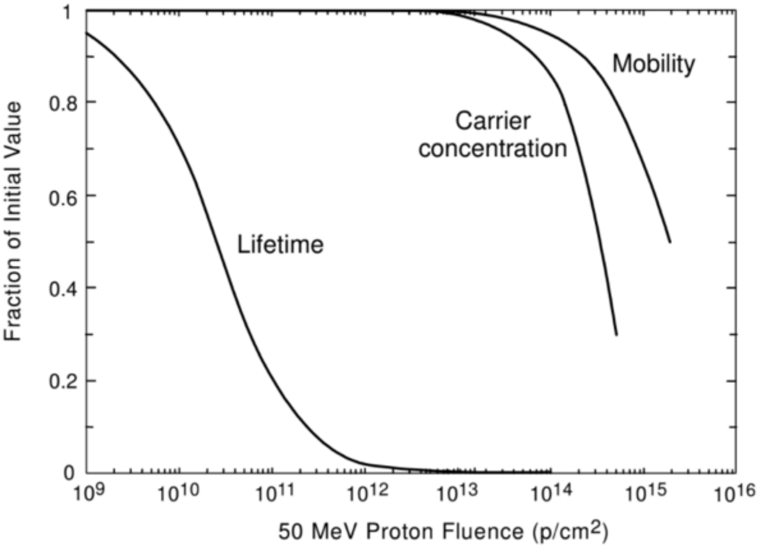

Figure 22. Degradation of Minority Carrier Lifetime, Carrier Concentration, and Mobility for GaAs Light-Emitting Diode. Source: [9].

D. ESTIMATION OF DEFECT INTRODUCTION RATES

When an electron with energy E encounters a material such as a solar cell, it loses energy by several processes, described previously. The change in E as a function of distance travelled in the material is called stopping power S. The total stopping power is the sum of the stopping powers due to several independent physical processes:

$$S = \left(\frac{dE}{dx}\right)_{Total} = \left(\frac{dE}{dx}\right)_n + \left(\frac{dE}{dx}\right)_e + \left(\frac{dE}{dx}\right)_r \tag{18}$$

where x is the distance travelled in the material and the subscripts n, e, and r represent nuclear, electronic, and radiation stopping power, respectively [28]. The loss of energy due to radiation is generally small and is neglected [28]. Electronic energy loss due to ionization is also be neglected in this section. The energy loss to displacement damage is represented by the nuclear stopping power term, which can be used to calculate the rate of introduction of displacements within the material [28].

1. Non-ionizing Energy Loss

The ability to compare different types of particles with varying energies is valuable in the prediction and modeling of radiation damage. A common method is by utilizing the non-ionizing energy loss (NIEL). The NIEL, also known as the nuclear stopping power, is obtained by combining all non-ionizing process together into a displacement damage dose that is deposited in the material [28]. Using the NIEL as a function of particle energy, we estimate the number of displaced atoms from an incoming particle fluence as

$$N_D = \frac{0.8(NIEL(E))\phi}{2E_d} \tag{19}$$

where N_D is the number of displaced atoms, which we call defects, ϕ is the particle fluence, and E_d is the material's displacement threshold energy [28]. Equation 19 is a form of a radiation damage model known as the modified Kinchin-Pease (K-P) model and takes into account the energy loss by PKAs. The calculation of NIEL from first principles is beyond the scope of this thesis. Calculations of NIEL in this thesis are obtained using the online SR-NIEL calculator [29].

2. Effects of Displacement Damage on Solar Cell Parameters

The rate of defect creation due to an electron fluence can be estimated with a closer look at carrier recombination. The current produced in a *p-n* junction's depletion region due to recombination I_{dr} can be approximated by

$$I_{dr} = -qA\left(\frac{kT}{2q\varepsilon_{\max}}\right)\left(\frac{n_i}{\tau}\right)e^{qV_A/2kT} = I_s e^{qV_A/2kT} \tag{20}$$

where A is the cell area, ε_{max} is the maximum electric field in the depletion region, n_i is the intrinsic carrier concentration, V_A is the applied voltage, I_s is the diode saturation current, and τ is the recombination lifetime which can be written as

$$\tau = \frac{1}{\sigma \nu_{th} N_R} \tag{21}$$

where σ is the capture cross section, v_{th} is the thermal velocity, and N_R is the concentration of recombination centers [30]. The diode saturation current I_s is equal to

$$I_s = qA\left(\frac{kTn_i}{2q\varepsilon_{\max}}\right)\sigma v_{th} N_R. \tag{22}$$

We note that the literature shows Equation 21 in different forms, but the most important relationship to show is that I_s is proportional to N_R. By using the modified K-P model and assuming parameters other than N_R in Equation 21 do not change with irradiation, we modify I_s as a function of electron fluence through the change in the concentration of recombination centers N_R introduced through radiation exposure. The concentration of recombination centers as a function of fluence $N_R(\phi)$ can be described by

$$N_R(\phi) = N_R(0) + \gamma_R \phi_e \tag{23}$$

where $N_R(0)$ is the initial concentration of recombination centers, γ_R is the defect introduction rate, and ϕ_e is the electron fluence [31]. From the derivations in Chapter II, the open circuit voltage of a solar cell is given by

$$V_{oc} = \frac{nkT}{q}\ln\left(\frac{I_{sc}}{I_s} + 1\right) \tag{24}$$

where n is the diode ideality factor and is equal to two for recombination by deep defects that exist near the midgap of E_g [8]. Using Equation 22, we define the change in V_{oc} due to an electron fluence to be

$$\Delta V_{oc}(\phi_e) = \frac{nKT}{q}\left(\ln\left(\frac{I_{sc}(\phi)}{I_{sc}(0)}\right) + \ln\left(1 + \frac{\gamma_R \phi_e}{N_R(0)}\right)\right) \tag{25}$$

where $I_{sc}(\phi)$ is the device short-circuit current as a function of fluence and $I_{sc}(0)$ is the un-irradiated device I_{sc} [31]. This change in V_{oc} is used in the results chapter to estimate the defect introduction rate as a function of electron fluence.

IV. SOLAR CELL MEASUREMENT SYSTEM DESIGN AND RADIATION TEST PLAN

In this chapter, we include a discussion of the equipment and methodology developed to characterize the radiation performance of solar cells examined in this thesis. The tests performed include illuminated DC current-voltage (IV) and EQE measurements.

A. SOLAR SIMULATOR 1000

One of the light sources used to measure the IV characteristics of the devices was the Solar Simulator 1000 and is referred to as the SS 1000 for the remainder of this thesis. The SS 1000 utilizes a 1600 W Xe lightbulb to simulate the solar spectrum and is shown in Figure 23.

Figure 23. SS 1000 with Dark Box Surrounding the Light Output

Before performing any measurements with the test devices, we characterized the light output by measuring its integrated power density (PD) and power spectral density (PSD) variation. The PD was measured with a HT204 handheld optical power meter at 17 locations in the beam as illustrated in Figure 24. The beam output covers an area of approximately 21 × 21 cm. The resulting PD variation is shown in Figure 25 with the center location set to a PD of 1,365 W/m^2 to simulate an AM0 spectrum by manually adjusting the current supplied to the bulb. The PD of the beam output varies significantly over the entire beam area; however, the test device, which is only 1.96 × 5 cm, was subjected to a PD of 1,365±20 W/m^2.

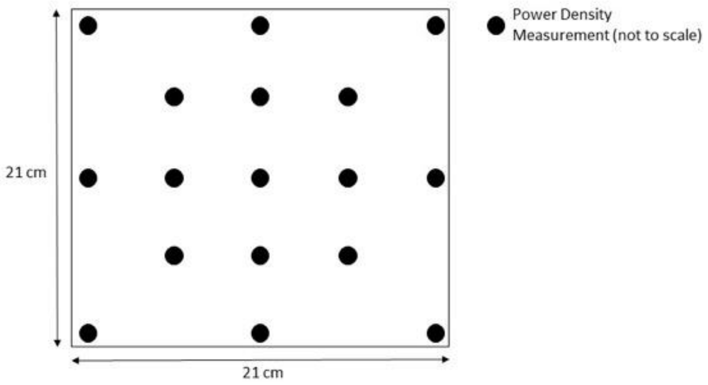

Figure 24. SS 1000 PD Measurement Locations

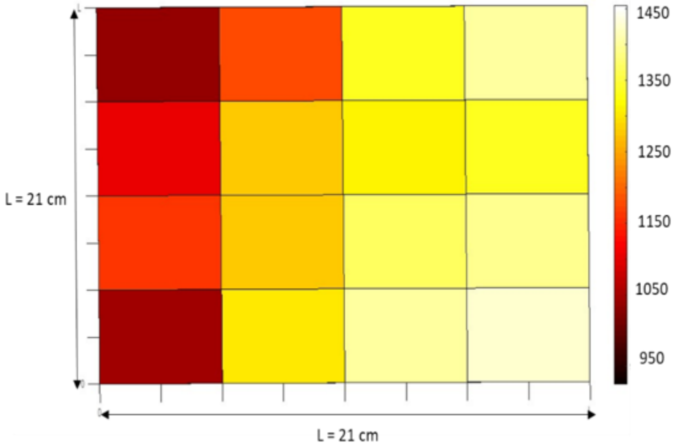

Figure 25. SS 1000 Beam Output PD Variation in W/m^2

The PSD was measured with a Newport model 1918-R Power Meter with an attached Si diode photodetector and Oriel Cornerstone 130 monochromator in the configuration as shown in Figure 26. A computer program called TracQ was used to step through each wavelength and measure the corresponding power density. The PSD was measured from 200 to 1,800 nm in wavelength.

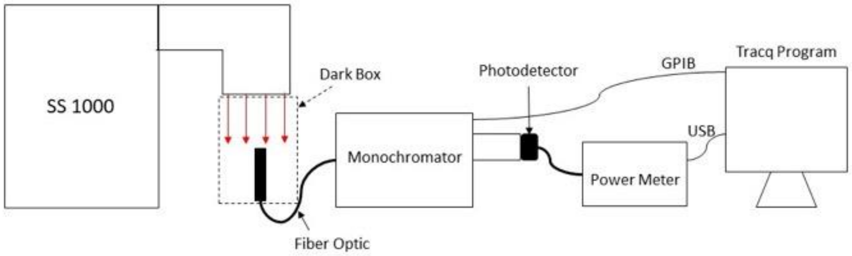

Figure 26. Block Diagram of PSD Measurement for the SS 1000

PSD was measured at five locations in the beam to determine spatial uniformity of the spectrum as shown in Figure 27. The shape of each measured location's spectrum was the same with overall magnitude being the only variation. The spectrum measured at the beam center is displayed in Figure 28.

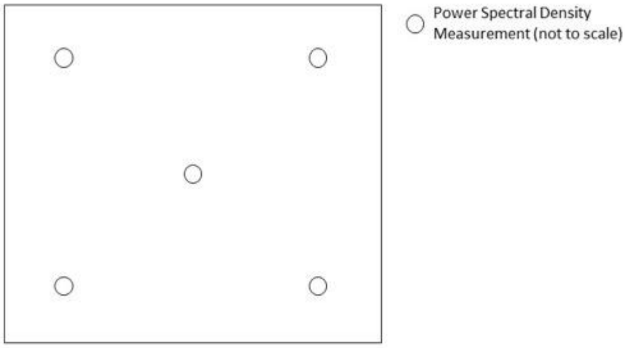

Figure 27. SS 1000 PSD Measurement Locations

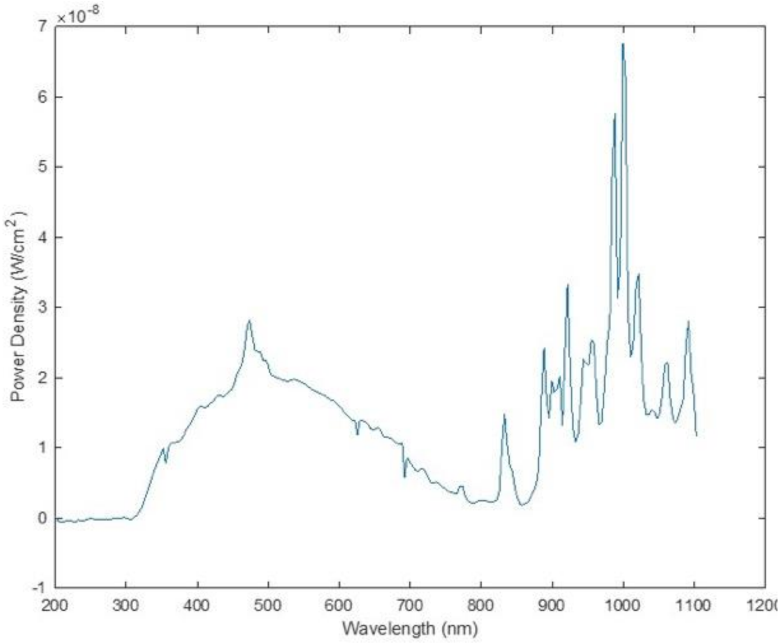

Figure 28. SS 1000 PSD at Beam Center from 200 nm to 1,100 nm

The measured PD per wavelength was reduced significantly due to the low light throughput of the fiber optic cable and monochromator. Corrections were applied by rescaling based upon the integrated intensity measured by the handheld meter.

Due to spectral mismatch between AM0 and the Xenon spectrum, the output spectrum of the solar simulator was not equivalent to an AM0 spectrum of the same integrated total intensity. The AM0 spectrum file used for this correction was the ASTM E-490 standard spectrum [32]. First, the AM0 spectrum was integrated over the same range as the Xe spectrum,

$$PD_{AM0} = \int_{\lambda_i}^{\lambda_f} PSD_{AM0}\, d\lambda \approx \sum_{\lambda=200}^{1800} PSD_{AM0}\Delta\lambda \tag{26}$$

where λ_i and λ_f are the initial and final wavelengths, respectively, corresponding to 200 nm and 1,800 nm, and $\Delta\lambda$ is the wavelength step size. Evaluating Equation 25 gave a total PD for AM0 of 1,235 W/m^2. Next, the PD of the measured Xe spectrum was calculated from

$$PD_{measured} = \sum_{\lambda=200}^{1800} PSD_{measured}\Delta\lambda \tag{27}$$

where $PSD_{measured}$ are the measured values of the SS1000 Xe spectrum, and the wavelength step size is the monochromator resolution of 3.7 nm. The $PSD_{measured}$ was then scaled by a power density correction factor C_{PD} by setting the PD of the Xe spectrum equal to PD_{AM0}

$$PD_{Xe} = PD_{AM0} = \left(C_{PD}\right) PD_{measured} \tag{28}$$

The scaled PD_{Xe} is shown with PD_{AM0} for reference in Figure 29. It is obvious that there is a large difference in spectrum shape when compared to AM0 for the region between 200 nm and 875 nm. This is an important distinction to make in regards to photon absorption.

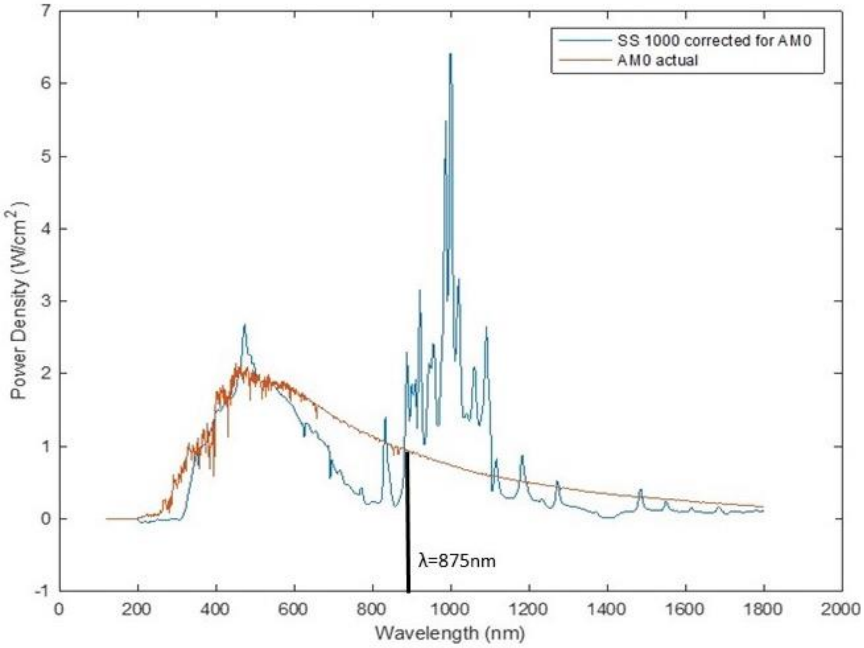

Figure 29. Corrected SS 1000 and AM0 Power Spectral Densities

As discussed previously, in order for an electron-hole pair to be created by photon absorption, the incoming photon must have an energy greater than or equal to E_g. GaAs has a bandgap energy of 1.42 eV at 300 K [8]. With the use of Equation 1, a photon must, therefore, have a wavelength less than or equal to 873 nm to create an electron-hole pair in GaAs. A method to account for the lack of power in the Xe spectrum for wavelengths less than 875 nm was used. The ratio of power spectral densities between the Xe and AM0 spectrum for wavelengths less than 875 nm leads to another correction factor,

$$CF = \frac{\sum_{\lambda=200nm}^{875nm} PSD_{AM0}\Delta\lambda_{AM0}}{\sum_{\lambda=200nm}^{875nm} PSD_{Xe}\Delta\lambda_{Xe}} \tag{29}$$

where $\Delta\lambda_{AM0}$ is the AM0 file wavelength step size and $\Delta\lambda_{Xe}$ is the monochromator resolution. The correction factor was calculated to be 1.3078, which is used in the results chapter for a better comparison of data.

B. XENON TUNABLE LIGHT SOURCE

The second light source used for IV measurements was a Newport Xe tunable light source (TLS), shown in Figure 30. The operation of this source is very similar to that of the SS 1000 except that it utilizes a 300 W Xe bulb. This light source, in conjunction with an Oriel Cornerstone 130 monochromator, was also used for EQE measurements.

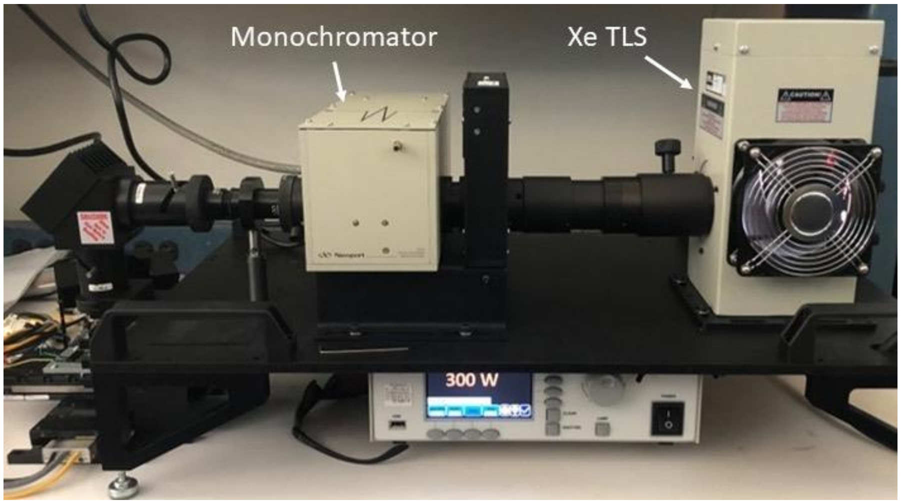

Figure 30. Xe TLS and Monochromator in the EQE Configuration

As with the SS 1000, the same PD and PSD measurements were taken to characterize the beam output of the Xe TLS. The PD was measured at four locations in the beam output as displayed in Figure 31. The PSD was measured at nine points in the beam output as shown in Figure 32.

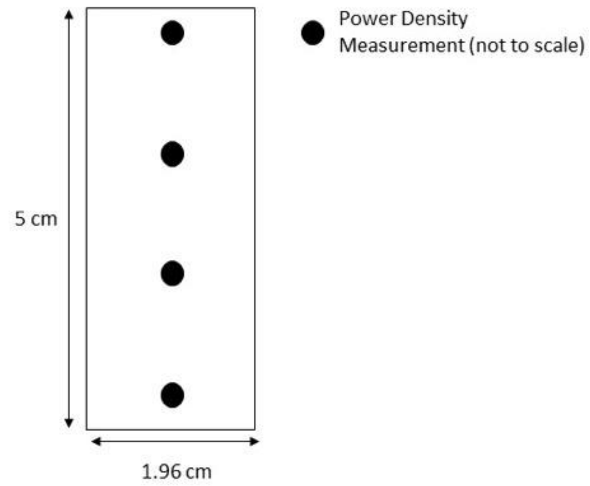

Figure 31. Xe TLS PD Measurement Locations

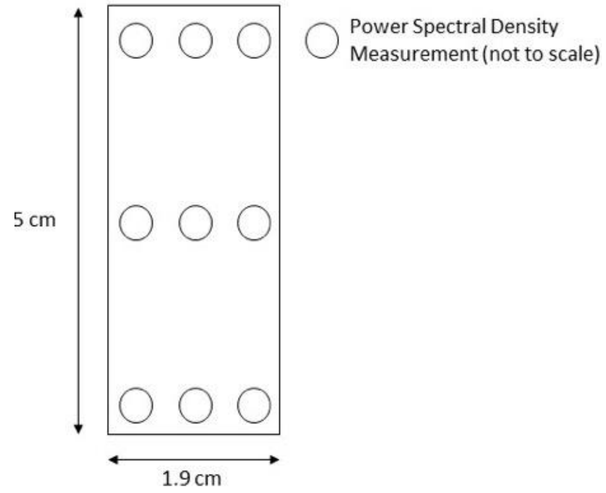

Figure 32. Xe TLS PSD Measurement Locations

In the set-up for the EQE measurements, it became apparent that the beam for the Xe TLS was non-uniform as seen in Figure 33.

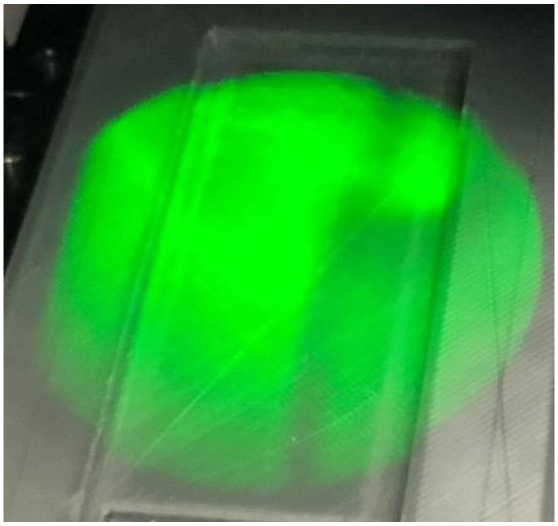

Figure 33. Xe TLS Beam Variation at 555 nm

In Equation 14, it was shown that the EQE is proportional to the ratio of photocurrent to incident photon flux or more generally, incoming light power as given by

$$EQE \propto \frac{I_{ph}}{P_{in}} \tag{30}$$

where P_{in} is the measured PSD of the light source. The incoming power can be represented by the integral of PSD at every location over the entire area of the beam given by

$$P_{in} = \int_{Area} P_{x,y}\, dA. \tag{31}$$

In order to properly measure the incoming power from the light, an average PSD was calculated using the nine points in Figure 32. The PSD was measured by a photodetector with a square centimeter exposed region, and P_{in} was approximated by the average of the nine measurements with

$$P_{in} \approx P_{avg} = \frac{\sum P_i}{N} \tag{32}$$

where P_i is the measured PSD at each location and N is the number of samples. The resulting PSD is given in Figure 34 and possesses the same shape as the SS 1000 PSD as expected.

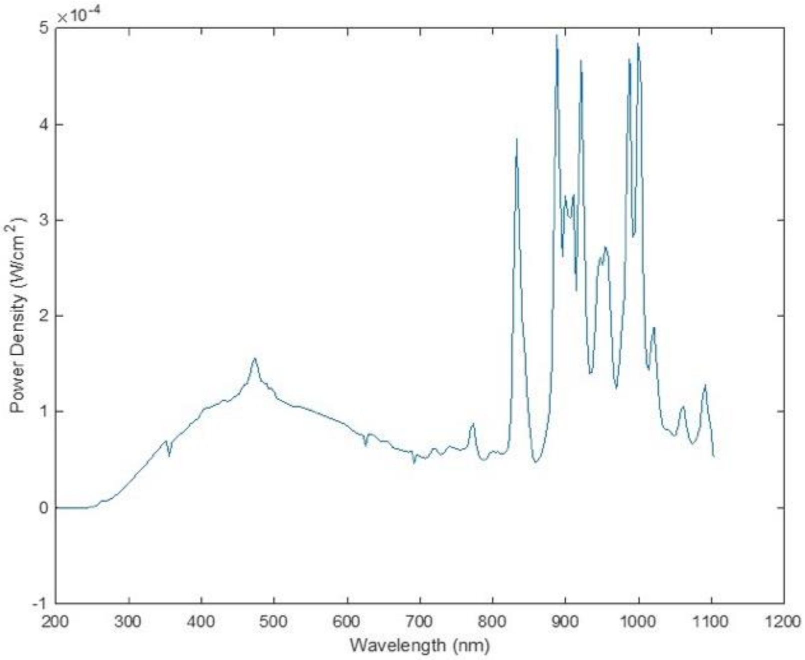

Figure 34. Xe TLS Average PSD

C. ILLUMINATED DC IV MEASUREMENTS

The performance of the IV measurements was completed using two different configurations. The initial measurements were performed with the set-up illustrated in Figure 35. This included the SS 1000 as the light source with the test device directly under the center of the beam which was manually adjusted to a PD of 1365 W/m^2 to simulate AM0. The test device outputs were connected to an HP 4142 high resolution source measurement unit (SMU). The SMU was connected via general purpose interface bus (GPIB) to a terminal with a Labview virtual instrument (VI) developed to control the test. The SMU measured current through the device as the applied voltage was swept from zero to 1.2 V in 0.01 V increments. In order to maintain the change in device temperature as small as possible while still acquiring a sufficient number of samples, ten current measurements were obtained at each step in voltage and averaged. The device temperature was measured prior to and immediately following the test with a Fluke 62 Mini IR handheld pyrometer. Additionally, the devices were placed inside a dark box to minimize background light pollution.

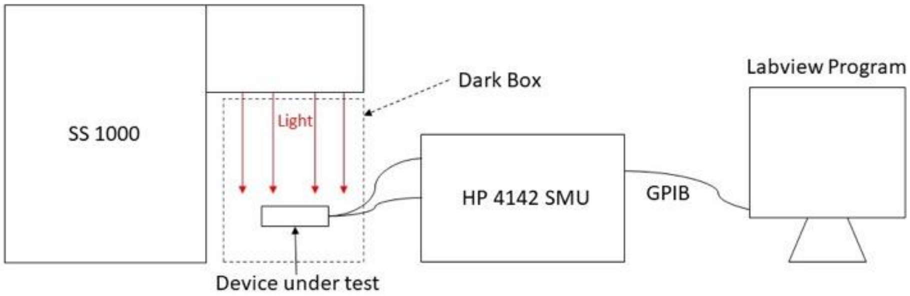

Figure 35. Block Diagram of IV Measurement System Using the SS 1000

The second IV measurement set-up was utilized on-site during radiation measurements for its ease in portability. This configuration is illustrated in Figure 36. The Xe TLS 300 W lamp was used as the light source with an Agilent B1510A High Power SMU as the instrument for applied voltage and measured current. Again, the change in temperature was measured with handheld pyrometer, and the light pollution was minimized by performing the tests in a dark room.

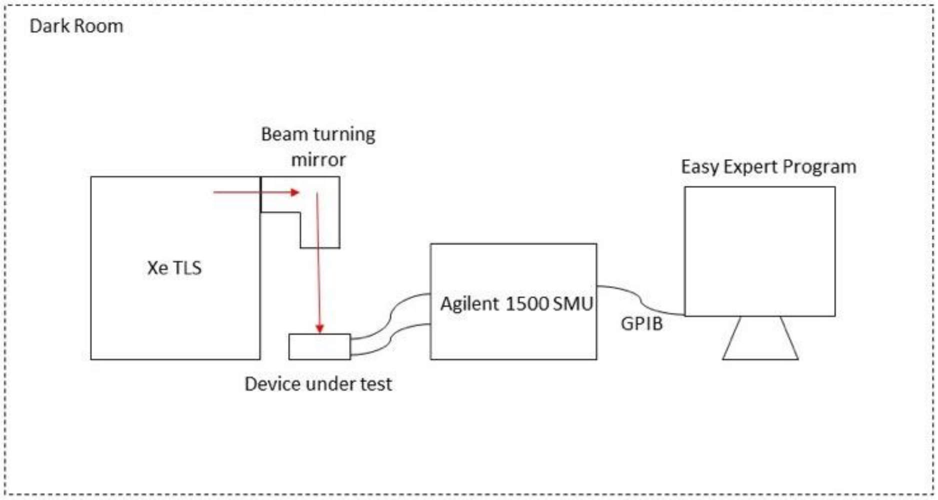

Figure 36. Block Diagram of IV Measurement Using the Xe TLS Lamp

The final IV measurement was the dark current measurement of each device which utilized the same configuration as shown in Figure 36 with the only exception being the cells were not illuminated. This measurement was performed prior to irradiation and for each intermediate step during the irradiation.

D. EQE MEASUREMENTS

As discussed in the solar cell fundamentals chapter, the EQE is a measure of the conversion efficiency of photons to electron-hole pairs within the solar cell as a function of wavelength. The actual set-up used to measure the EQE was shown earlier in Figure 30, and a block diagram illustrating the configuration is in Figure 37.

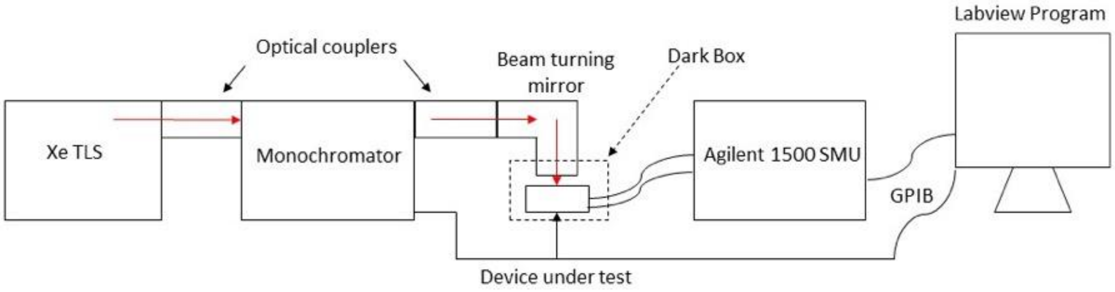

Figure 37. Block Diagram of the EQE Measurement System

From Equation 14, we see that the EQE is the ratio of the electron production rate to the rate of incoming photons in a solar cell. The electron production rate is given by

$$\frac{electrons}{\mathrm{s}} = \frac{1}{q} I_{ph} \tag{33}$$

where I_{ph} is the measured photocurrent from the SMU. The rate of incoming photons is determined by

$$\frac{photons}{\mathrm{s}} = \frac{A_{cell} PSD_{measured}}{E_{ph}} \tag{34}$$

where A_{cell} is the solar cell area, $PSD_{measured}$ is the average PSD of the Xe TLS output, and E_{ph} is the energy of a photon, which is given by Equation 1.

For the performance of the test, the Xe TLS used with a minimum resolution of 3.7 nm to apply varying wavelengths of light to the solar cell between 200 nm to 920 nm. Photocurrent developed by the cell was measured using an Agilent B1510A High Power

SMU while the solar cell contacts were shorted by applying zero voltage through the SMU. A Labview VI was developed to control the test, and the front panel of this VI is shown in Figure 38. The entire Labview VI for EQE measurement is given in Appendix A. The power of the incoming light was low enough that temperature did not change appreciably during the test; therefore, 100 measurements per wavelength step were taken. Additionally, another dark box was used to minimize background light pollution.

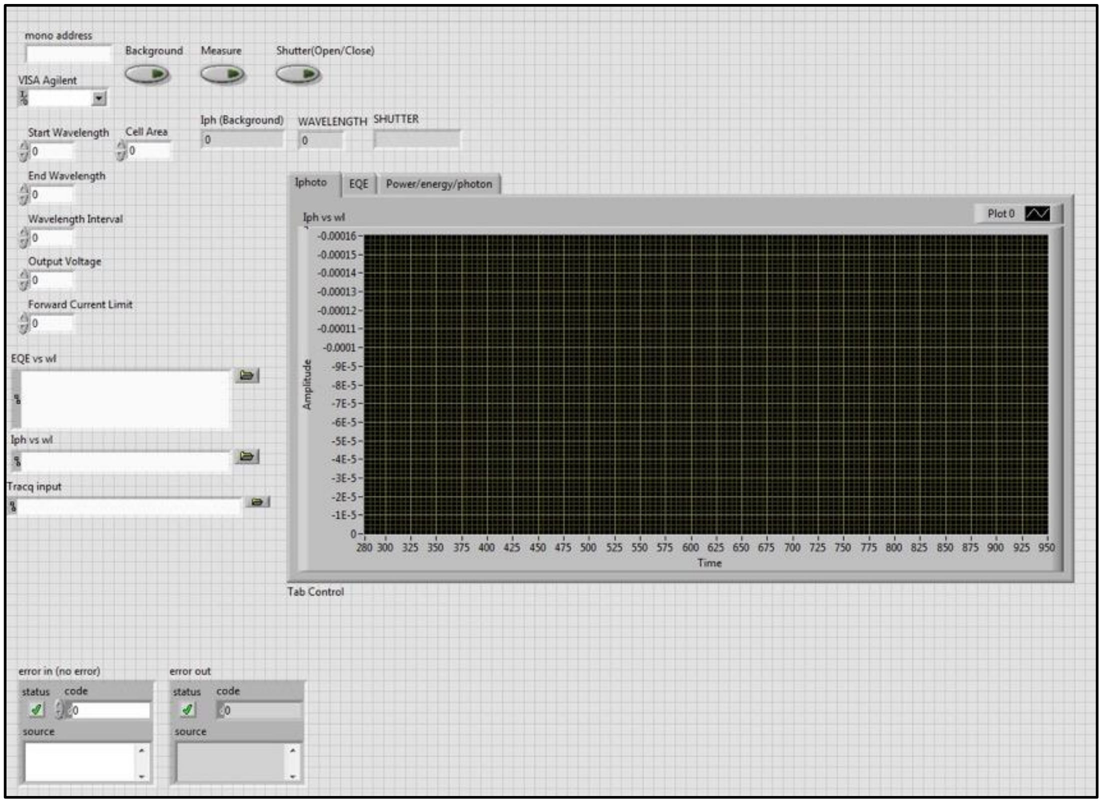

Start Wavelength 0
Cell Area 0
End Wavelength 0
Wavelength Interval 0
Output Voltage 0
Forward Current Limit 0
Iph (Background) 0
WAVELENGTH 0
error in (no error) code 0
error out code 0

Figure 38. Labview VI Front Panel Used for EQE Measurement Control

E. CAPACITANCE-VOLTAGE MEASUREMENTS

In order to determine the doping density of the bulk material in the test devices, capacitance-voltage (C-V) measurements were performed. By treating the depletion region as a parallel plate capacitor and following the derivation in [12], it can be shown that the doping concentration can be calculated from C-V measurements via

$$N_A = \frac{2/qK_s}{A^2 \frac{d(1/C^2)}{dV}} \tag{35}$$

where N_A is the concentration of donor acceptors in the *p*-type bulk material of the cell, K_s is the dielectric constant of the material, A is the cell area, and C is the measured capacitance of the depletion region.

This measurement was performed after irradiation, and the device with the lowest total fluence was used. A capacitance measurement unit (CMU) was used with the Agilent B1500 to produce a 30-mV AC signal at 1.0 kHz. The resulting slope of the $1/C^2$ versus V curve corresponds to a doping density of approximately 10^{17} cm^{-3} in the *p*-type material. The doping density is used in Chapter V to estimate the defect introduction rate.

THIS PAGE INTENTIONALLY LEFT BLANK

V. RESULTS

A. ALTA THIN-FILM GAAS SOLAR CELLS

The devices tested were single-junction GaAs solar cells fabricated by Alta Devices, Inc. These cells were fabricated using an MOCVD grown layer using ELO to form the thin film, as described in Chapter II. Each cell measured 1.96 × 5.0 cm with an exposed region of GaAs of 1.71 × 5.0 cm.

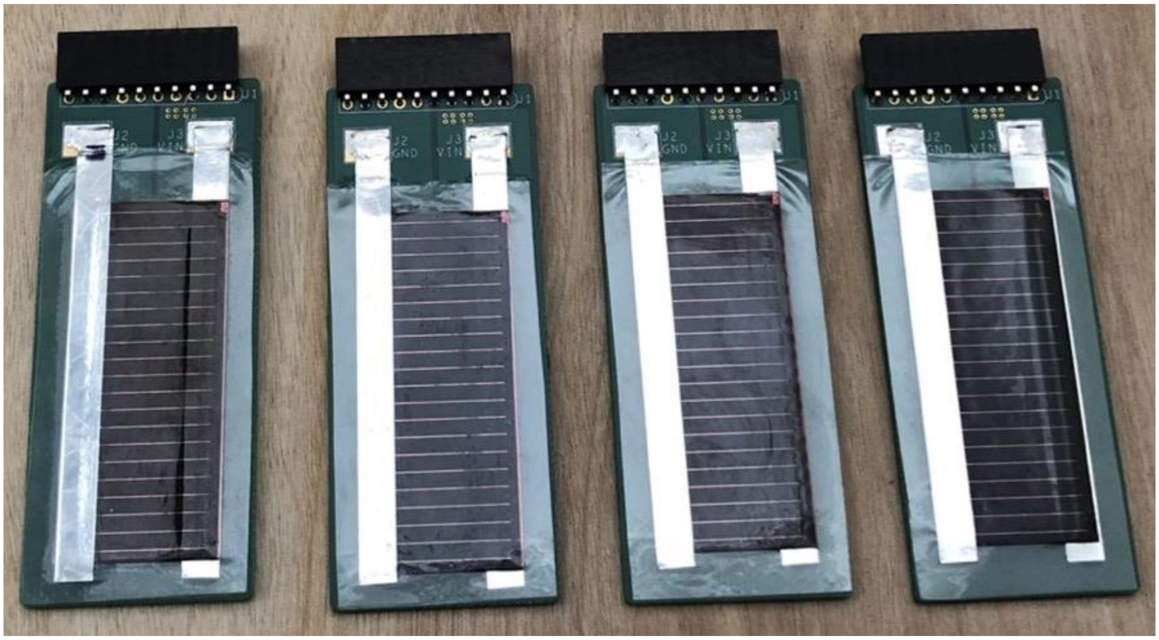

Figure 39. Single-Junction Thin-Film GaAs Solar Cells Tested in this Research

The cells were received individually packaged and mounted on a printed circuit board (PCB). Additionally, a transparent plastic laminate completely sealed the cells for safe handling during the manufacturing process [18]. In total, five devices were obtained; however, during an attempt to remove a cell from the laminate, it was damaged and became inoperable. The decision was made to keep the cells intact on the PCBs, which left four test devices labeled A through D that are referred to in the following chapters and shown in Figure 39. The expected characteristics for these cells as provided by Alta Devices are displayed in Table 3.

Table 3. Alta Devices Self-Published Single-Junction GaAs Characteristics. Adapted from [33].

Electrical Characteristics	**Units**	**AM1.5, 25°C**	**AM0, 25°C (estimated)**
Efficiency (PCE)	[%]	26	23
Power per cell (shingled)	[W]	0.22	0.26
Open Circuit Voltage (Voc)	[V]	1.10	1.12
Short Circuit Current (Isc)	[mA]	240	273

B. RADIATION TEST PLAN

The majority of all electron radiation research for solar cells takes place at an energy of 1.0 MeV to simulate the energy of particle radiation in Earth orbit. The goal of this thesis is to evaluate the effects of electron radiation at a significantly higher energy. Solar cells can be exposed to much higher energies than 1.0 MeV in a realistic space environment, as discussed in Chapter III. A LINAC that can produce the energy desired was required. Radiation exposure of tested solar cells was performed at the Idaho Accelerator Center (IAC) in Pocatello, ID which is operated by Idaho State University. The IAC houses several LINACs with one that can produce an electron beam at energies between 4.0 and 25.0 MeV. Originally, the tests were planned for 22.0 MeV; however, there was concern of excessive heating of the PCBs on which the cells were mounted which could cause damage to the cells not directly attributed to the incoming electron beam. The tests were performed at 8.0 MeV, which is still significantly higher than the standard 1.0 MeV, and excessive heating did not occur. The temperature change during the irradiation was not measured using the base assumption that the 8.0 MeV beam would not cause appreciable heating of the thin film solar cell which was measured via scanning electron microscope to be around three microns thick.

With only four devices, a test plan was devised to maximize the data points obtained. The test plan is illustrated in Figure 40 with the measurement steps listed in Table 4. The LINAC has the capability of emitting a single pulse of electrons which the operators can measure by accumulated charge. This charge is collected through an aluminum block which can be used to determine the electron fluence per pulse by

$$\frac{fluence}{pulse} = \frac{electrons/cm^2}{pulse} = \frac{Q_{accum}\left(\frac{1}{q}\right)}{A_{block}} \tag{36}$$

where Q_{accum} is the total charge accumulated in the aluminum block in coulombs and A_{block} is the area of the block in cm^2. With the LINAC tuned to 8.0 MeV, the accumulated charge per pulse was 91 nC, and the area of the block was 15.75 cm^2. The electron fluence per pulse was 3.6×10^{10} cm^{-2}.

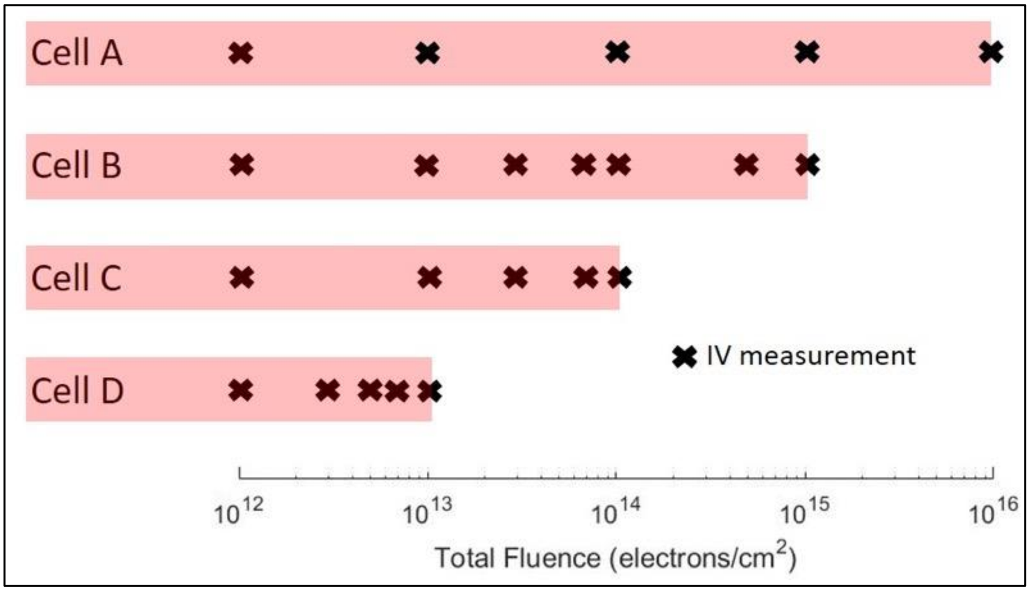

Figure 40. Illustration of Radiation Test Plan for all Test Devices

Once the number of electrons per pulse was known, the desired number of pulses for each cell was determined. The fluence for each cell is cumulative; therefore, the number of total pulses to each cell was tracked to ensure the test compliance was met.

Table 4. Radiation Test Plan Listing Intermediate Measurement Steps

Cell	**Measurement Steps (electrons/cm^2)**						
A	10^{12}	10^{13}	10^{14}	10^{15}	10^{16}	n/a	n/a
B	10^{12}	10^{13}	3×10^{13}	7×10^{13}	1×10^{14}	5×10^{14}	10^{15}
C	10^{12}	10^{13}	3×10^{13}	7×10^{13}	1×10^{14}	n/a	n/a
D	10^{12}	3×10^{12}	5×10^{12}	7×10^{12}	10^{13}	n/a	n/a

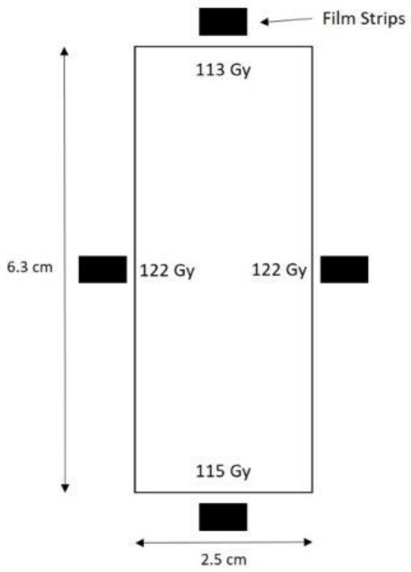

Figure 41. LINAC Electron Beam Uniformity Measurement Configuration

After the beam fluence per pulse was measured, the uniformity needed to be determined. The operators utilized a dosimetry film in the configuration shown in Figure 41. The measurement was in units of gray (Gy), and the variation in beam intensity was at a maximum, 7.96%.

C. CURRENT-VOLTAGE CHARACTERISTICS PRE- AND POST-IRRADIATION

Data obtained by IV measurements taken prior to irradiation with the SS 1000 and the 300-W Xe lamp and IV measurements taken during intermediate steps and after irradiation with the Xe lamp are presented in the following section. With this data, several characteristics were examined as a function of electron fluence, including I_{sc}, V_{oc}, maximum power $P_{\max}$, and change in V_{oc}. These parameters are normalized to pre-irradiation values by plotting the remaining factor R_F for each. A R_F is given by

$$A_{RF} = \frac{A_{rad}}{A_o} \tag{37}$$

where A_{rad} is the value after irradiation and A_o is the initial value prior to irradiation. The figures later in this chapter display the degradation of individual solar cell properties due to total electron fluence.

1. IV Measurement before Irradiation

The IV characteristics of all four devices prior to irradiation are shown in Figure 42. These measurements were taken using the SS 1000 as the light source and the HP 4142 as the SMU.

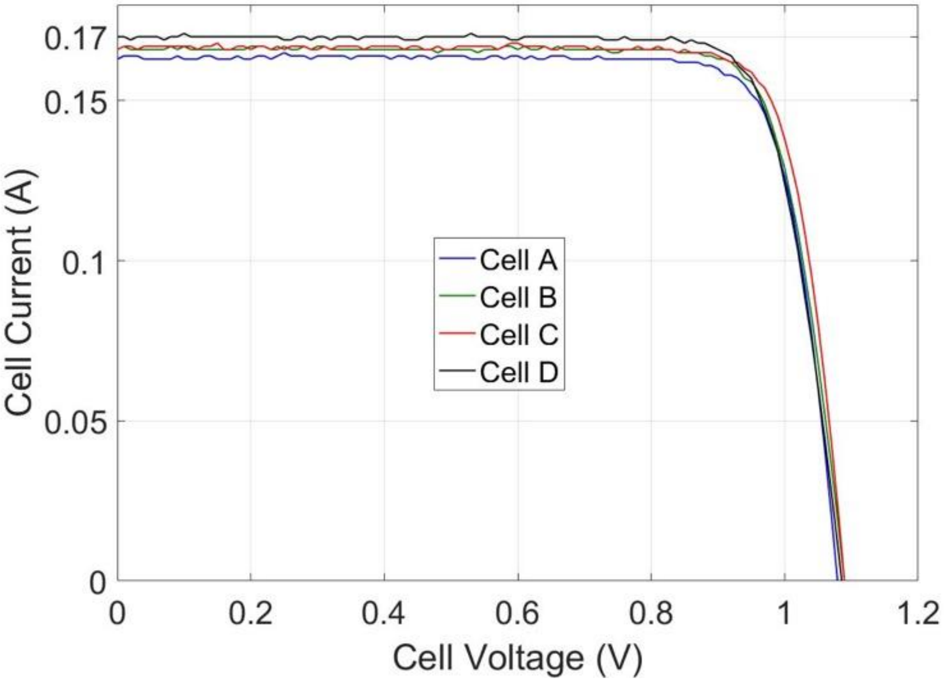

Figure 42. IV Characteristics of all Cells before Irradiation Using the SS 1000

It is very apparent when comparing the measured values to those claimed by Alta Devices in Figure 43 that the photocurrent I_{ph} is significantly lower for cells A through D. As discussed in the methods section, a correction factor for the spectrum differences between AM0 and the Xe lamps was calculated, and the resulting corrected parameters are shown in Table 5. For the purpose of this thesis, the overall performance of the cells is of little importance, and the relative performance of each cell when compared to the initial values is the focus.

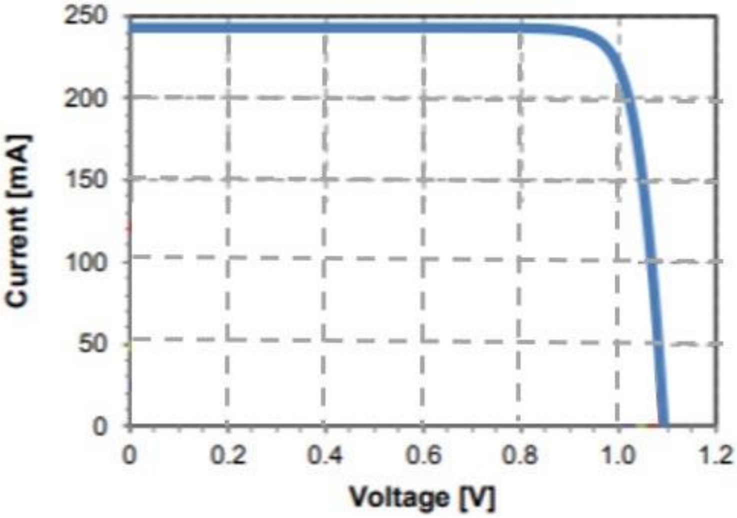

Figure 43. IV Characteristics of Alta Devices Single-Junction Solar Cell. Adapted from [33].

Even with the spectrum correction factor implemented, the test devices are seen to be of a lower quality than the advertised performance given by the manufacturer. This could be due to several factors, such as reflectance of the plastic laminate or due to premature degradation and aging of the cells prior to their reception at NPS.

Table 5. Test Device Parameters Corrected for AM0 Spectrum with Alta Devices Estimated Values at AM0 for Comparison. Adapted from [33].

Cell	**Isc [mA]**	**Voc [V]**	**F_F**	**PCE [%]**	**Pmax [W]**
A	213.6	1.08	0.83	18.17	0.191
B	217.5	1.09	0.82	18.53	0.194
C	217.5	1.09	0.83	18.80	0.197
D	222.2	1.09	0.81	18.74	0.196
Cell avg	217.7	1.09	0.82	18.56	0.195
Alta(est)	286	1.12	0.83	23	0.265

2. IV Measurement after Irradiation

The IV characteristics of each cell post-irradiation were measured using the Xe TLS as the light source and the Agilent B1500 for the SMU. The results for all four devices at their total electron fluence with the average IV plot prior to irradiation is shown in Figure 44. The degradation becomes very significant for a fluence greater than 10^{13} cm^{-2} and occurs in both the I_{sc} and V_{oc}. Although the device current was reduced to nearly zero for a fluence of 10^{16} cm^{-2}, it is important to note that the device did not completely fail and the IV characteristics were still measurable.

At intermediate steps during the irradiation, IV measurements were taken to obtain more data points and gain a better resolution of the degradation occurring. The individual cells and their intermediate measurements are shown in Figures 45 through 48. It can be seen that there is little damage occurring at a fluence of 10^{12} cm^{-2}, and the damage only has a small measurable effect on V_{oc}. As the fluence is increased, degradation of both I_{sc} and V_{oc} occurs.

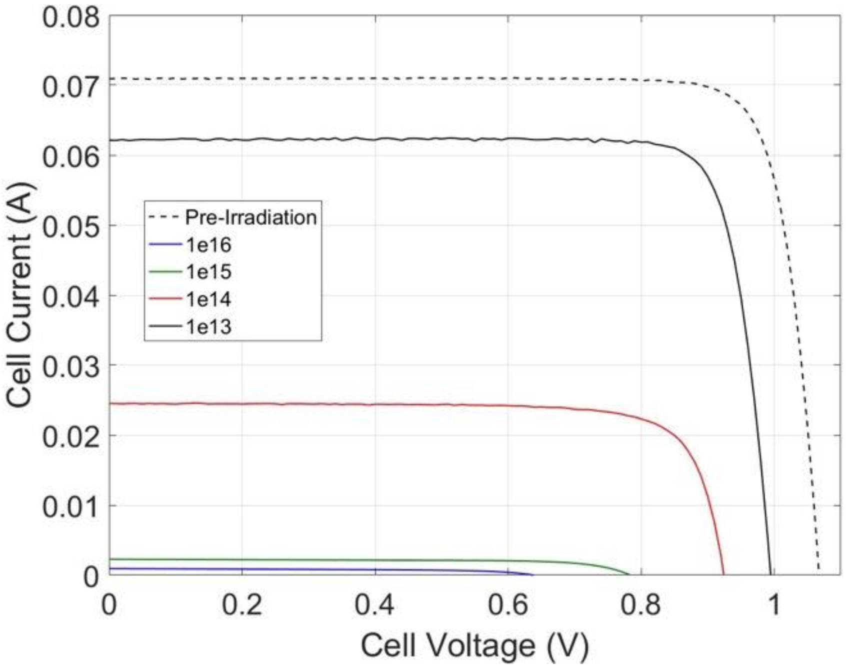

Figure 44. IV Characteristics of all Cells after Irradiation

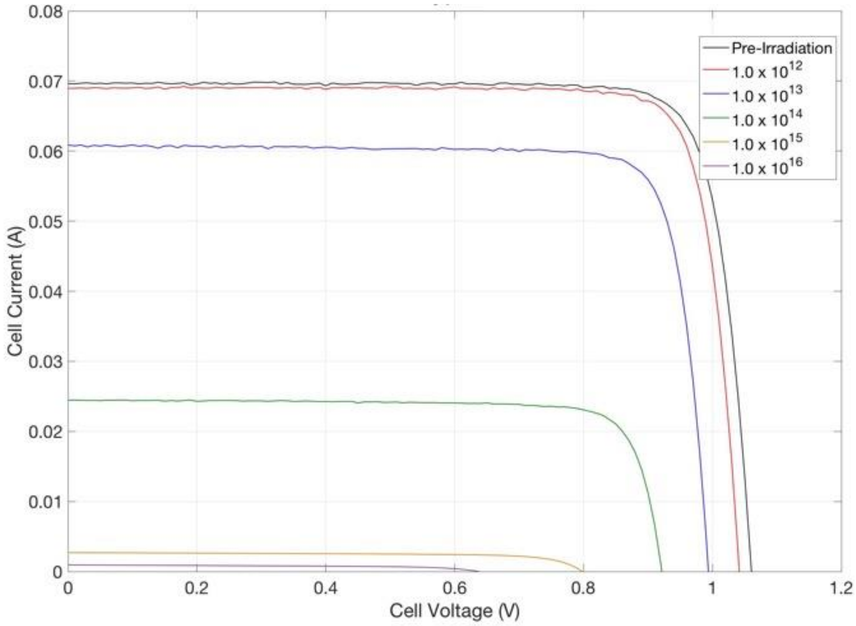

Figure 45. IV Characteristics for Cell A at Different Fluences

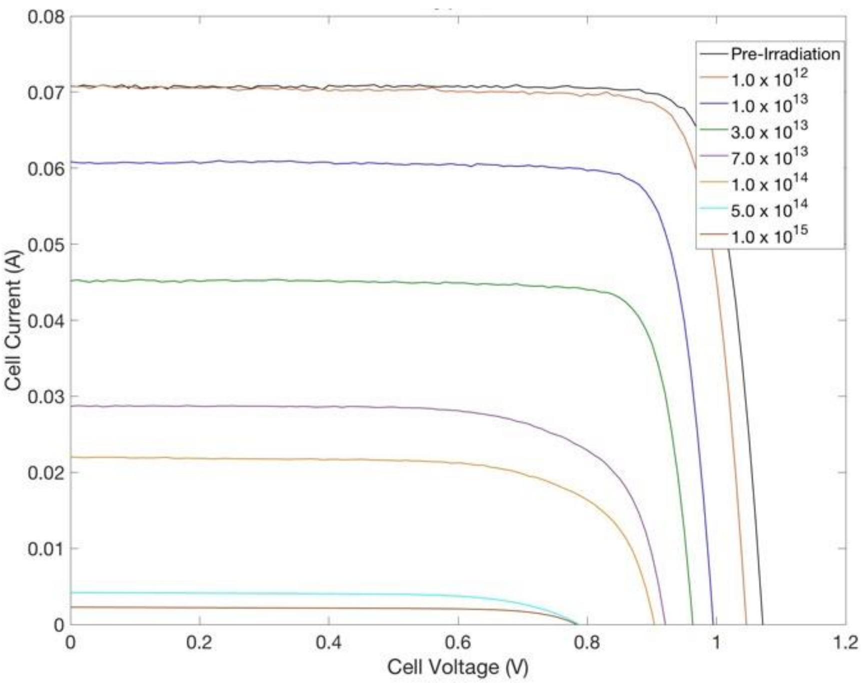

Figure 46. IV Characteristics for Cell B at Different Fluences

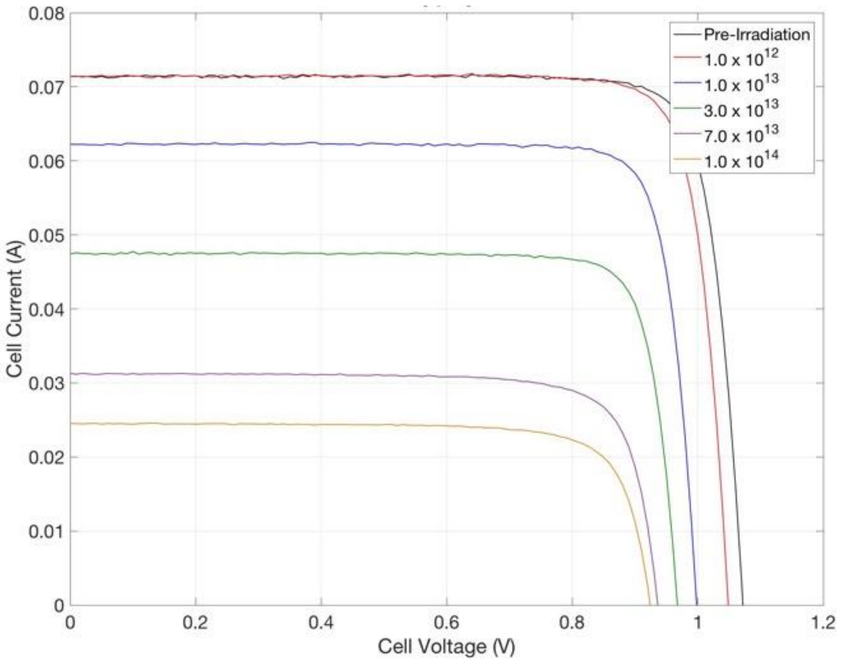

Figure 47. IV Characteristics for Cell C at Different Fluences

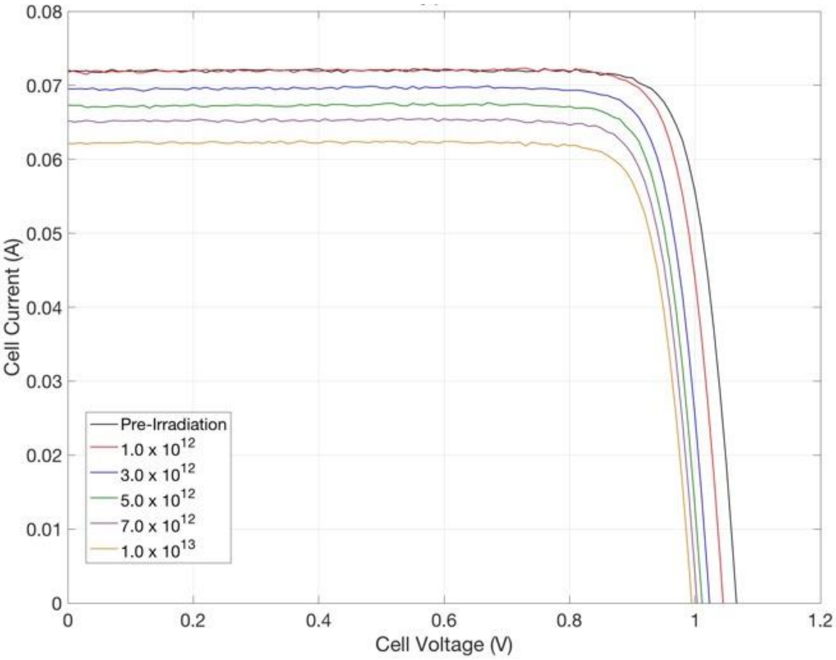

Figure 48. IV Characteristics for Cell D at Different Fluences

3. Temperature Change

During the measurements the devices were exposed to a high-power light which can produce a substantial amount of heat. For this reason, the time spent exposed to the light was minimized while still being long enough to obtain quality data. The change in temperature was recorded for each IV measurement, and the results are shown in Table 6.

Table 6. Change in Temperature and Corresponding Change in V_{oc} (estimated) for IV Measurements

Light Source	**SS 1000**	**TLS**
ΔT [K]	2 ± 0.5	2.5 ± 0.5
ΔVoc [mV]	-3 to -5	-4 to -6

As shown in [16], the temperature dependence of V_{oc} for GaAs is approximately 2.0 mV/K. This small difference in temperature was consistently reproduced and only changes the V_{oc} by a maximum of 0.006 V; therefore, it was considered negligible.

4. I_{sc} Remaining Factor

The change in I_{sc} as a function of total fluence is shown for all cells in Figure 49. The degradation from 10^{13} cm^{-2} to 10^{15} cm^{-2} is over 80% of the initial short circuit current, and each device appears to follow this trend as a function of total fluence. This decrease in current is by far the dominant source of performance reduction in these test devices.

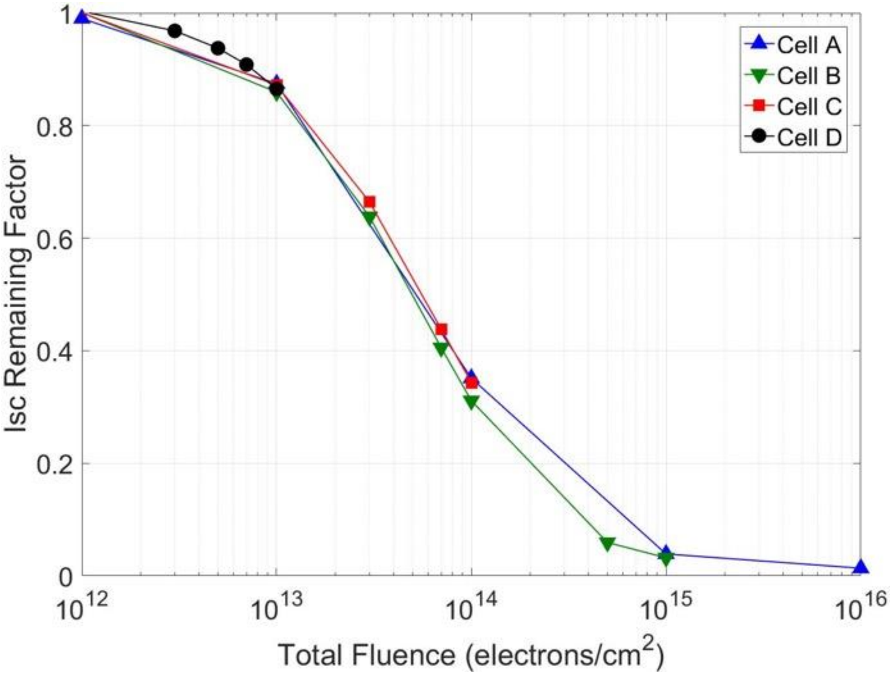

Figure 49. I_{sc} Remaining Factor as a Function Total Fluence

5. V_{oc} Remaining Factor and ΔV_{oc}

The V_{oc} R_F as a function of total fluence is shown for all cells in Figure 50. The reduction in V_{oc} is nearly linear on the logarithmic scale of fluence until 10^{14} cm^{-2}. The degradation shows the effect is magnified for a fluence larger than 10^{14} cm^{-2}, and the V_{oc} is reduced more quickly than for a lower fluence. At a total fluence of 10^{16} cm^{-2}, the V_{oc} is still approximately 60% of its original value. Again, all four devices followed the same overall trend in degradation. When compared to the effect on I_{sc}, the decrease in V_{oc} has a smaller effect on overall reduction of device performance.

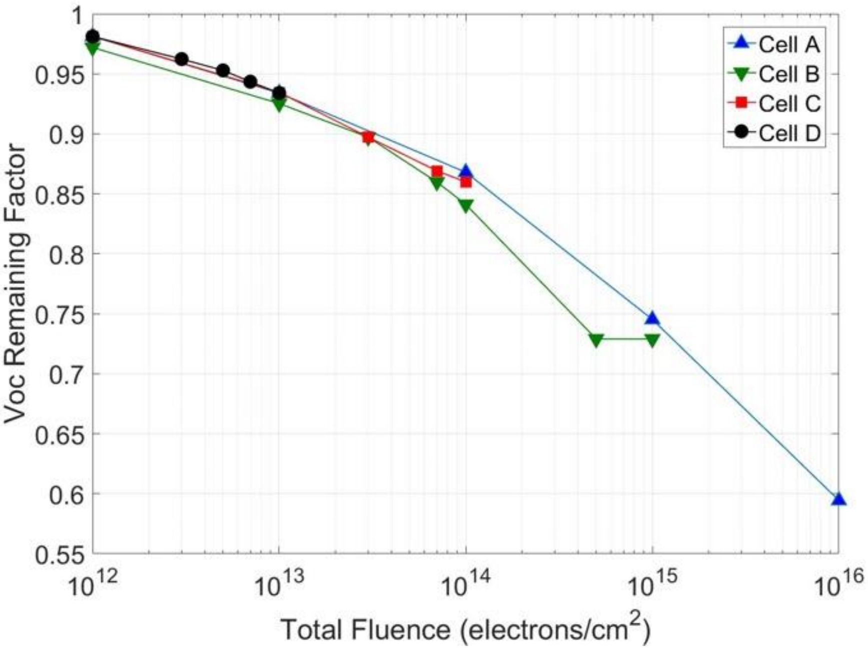

Figure 50. V_{oc} Remaining Factor as a Function of Total Fluence

6. Power Remaining Factor

The maximum output power R_F as a function of total fluence is shown in Figure 51. This factor has a similar shape to the I_{sc} R_F, which is expected as it is directly proportional to the current of the solar cell; however, as the maximum power of the device is a product of current and voltage, the degradation in device output power is greater than that of I_{sc} or V_{oc} alone. At a fluence of 10^{14} cm^{-2}, the cell output has been reduced to about 20% of what it was initially, and by 10^{15} cm^{-2}, the cells have been reduced to about 2.5% of their initial output. This degradation is very significant.

Measurements of the power remaining factor of similar GaAs thin-film cells under 1.0 MeV irradiation as a function of dose is shown in Figure 52. The power remaining factor for the cells exposed to 1.0 MeV electrons is still close to 50% after 10^{16} cm^{-2}, where the cells exposed to 8.0 MeV electrons in this work reach less than 50% two decades before that. At 10^{14} cm^{-2} and by 10^{16} cm^{-2}, the power remaining is less than 2%.

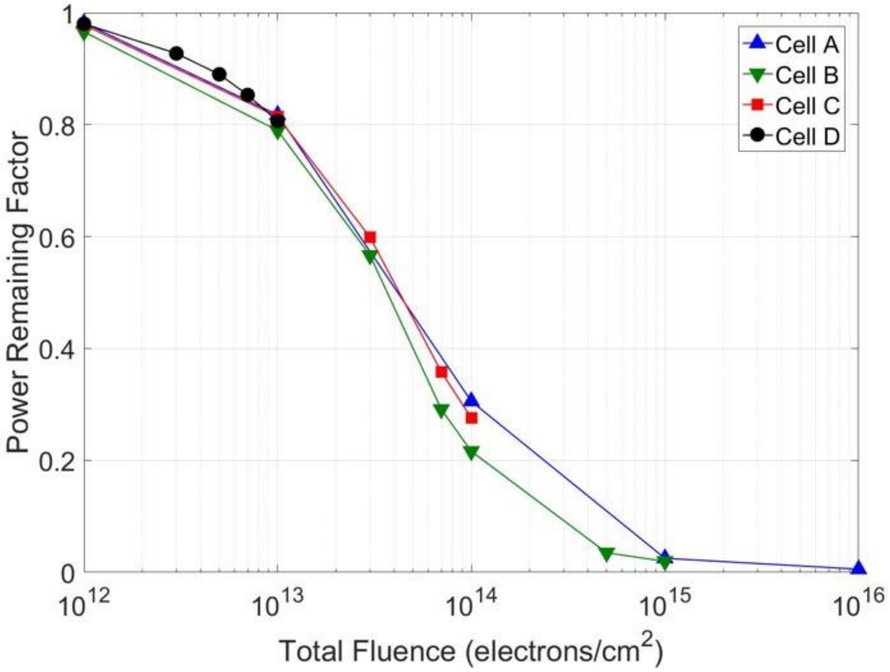

Figure 51. Maximum Power Remaining Factor as a Function of Total Fluence

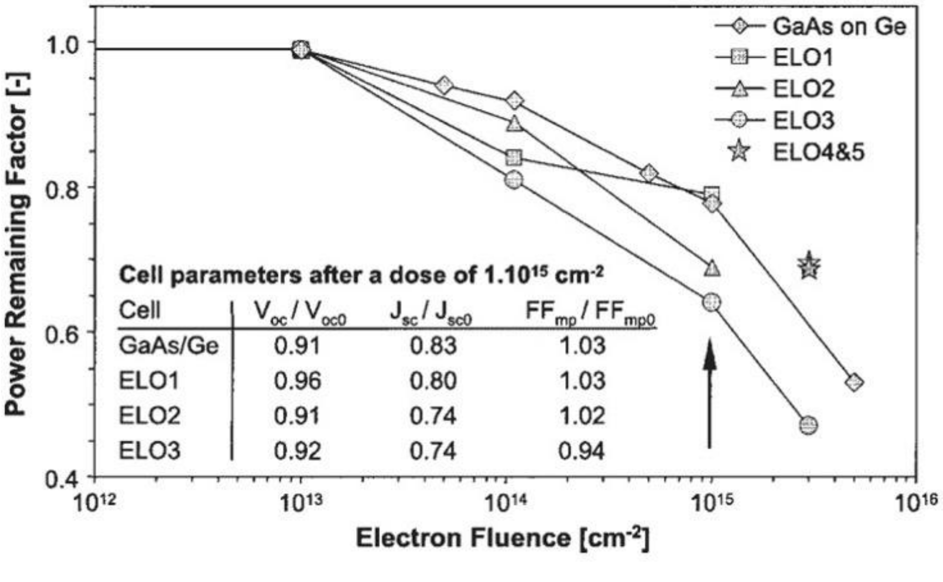

Cell parameters after a dose of 1.10^{15} cm^{-2}

Cell	V_{oc} / V_{oc0}	J_{sc} / J_{sc0}	FF_{mp} / FF_{mp0}
GaAs/Ge	0.91	0.83	1.03
ELO1	0.96	0.80	1.03
ELO2	0.91	0.74	1.02
ELO3	0.92	0.74	0.94

Figure 52. Power Remaining Factor as a Function of 1.0-MeV Electron Fluence for Thin-Film GaAs Solar Cells. Source: [19].

D. EQE

In the following section we display the results of the EQE measurements before and after irradiation. The EQE measurement system was disassembled in order to use the Xe TLS as the light source for measurements during and after the radiation test. This required the EQE system to be reassembled and aligned for the post-irradiation measurements. The average PSD was again measured but resulted in a more uniform beam than previously used. This would be problematic if exact differences in quantum efficiency were desired; however, the more important result for this thesis is the relative difference between fluence levels in order to determine regions of damage versus device thickness.

1. EQE before Irradiation

The measured EQE for all test devices prior to irradiation is displayed in Figure 53. There are small differences between all four cells, but the overall features are consistent.

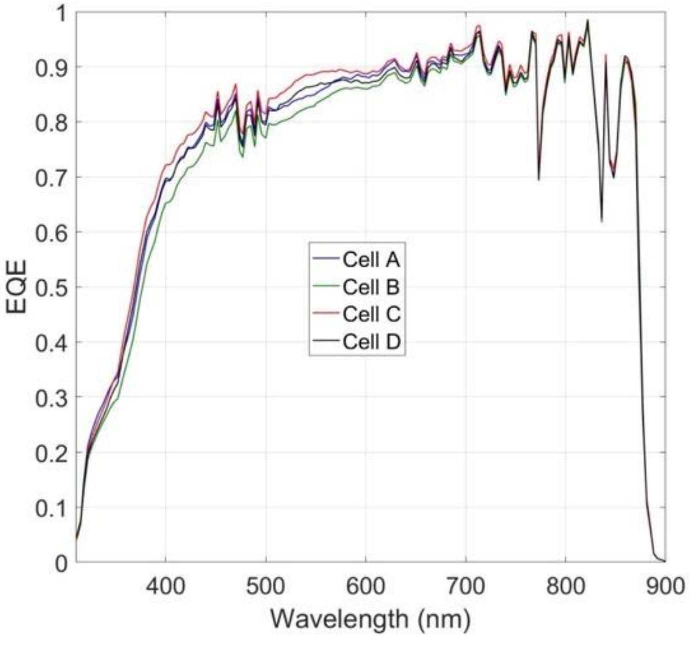

Figure 53. EQE of all Cells before Irradiation

The cells showed a measurable response between the wavelengths of 300 and 890 nm. The region around 700 nm shows a higher quantum efficiency than that around 500 nm by around 0.1, which indicates that the device is slightly more effective at utilizing photons for electron-hole pair production in the bulk material than at the surface.

2. EQE after Irradiation

The measured EQE post irradiation is shown in Figure 54 and reveals the regions of damage due to radiation as a function of device thickness. With a total fluence of 10^{13} cm^{-2}, the EQE shows a slight improvement at lower wavelengths when compared to the values before irradiation. This result is unexpected and points to a possible irregularity between the Xe spectrums used as the power input before and after the radiation tests. As mentioned before, the EQE experimental set-up required reassembly and alignment for the measurements in Figure 54, and the resulting averaged spectrum may have been slightly different.

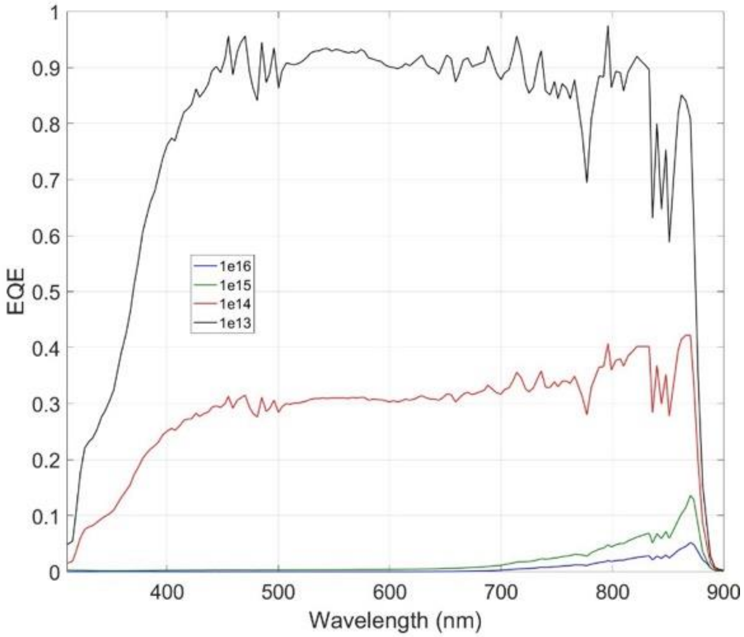

Figure 54. EQE of all Cells Post-Irradiation

The comparison between the 10^{13} cm^{-2} and the larger total fluences shows that the damage occurs primarily at depths in the device closer to the surface. This is very apparent for the 10^{15} cm^{-2} and 10^{16} cm^{-2} measurements where the device is not absorbing any photons below wavelengths of 600 nm.

The EQE post-irradiation still shows the jagged appearance as it did before. To gain a better understanding of the cause of this feature, different monochromator resolutions and bare cells without the plastic laminate should be tested in the future. It should also be noted that the laminate did not show any darkening or discoloration at any time during the test, thereby reducing the transmittance of light to the cell surface.

E. DEFECTS CREATED

The results of ΔV_{oc} are displayed in Figure 55 with a non-linear fit model of the form

$$\Delta V_{oc}(f_e) = \frac{nKT}{q}\ln\left(\frac{I_{sc}(f)}{I_{sc}(0)}\right) + \frac{nKT}{q}\ln\left(1 + Bf_e\right) \tag{38}$$

where B is $\gamma_R/N_R(0)$ and $N_R(0)$ is the initial concentration of recombination centers or defects prior to irradiation. This factor was calculated for all four devices, and the average was found to be 1.094×10^{-12} cm^2.

The initial concentration of native defects is unknown for these cells, and the utilization of a method such as deep level transient spectroscopy (DLTS) is required to measure this value for $N_R(0)$. Watanabe performed DLTS of pure GaAs, which was grown via MOCVD in a very similar fashion to the four test devices in this thesis [34]. The values measured in [34] for un-doped GaAs ranged from 2.1 to 3.8×10^{14} cm^{-3}. The average value of 3.1×10^{14} cm^{-3} was used as the initial concentration of defects for the test devices.

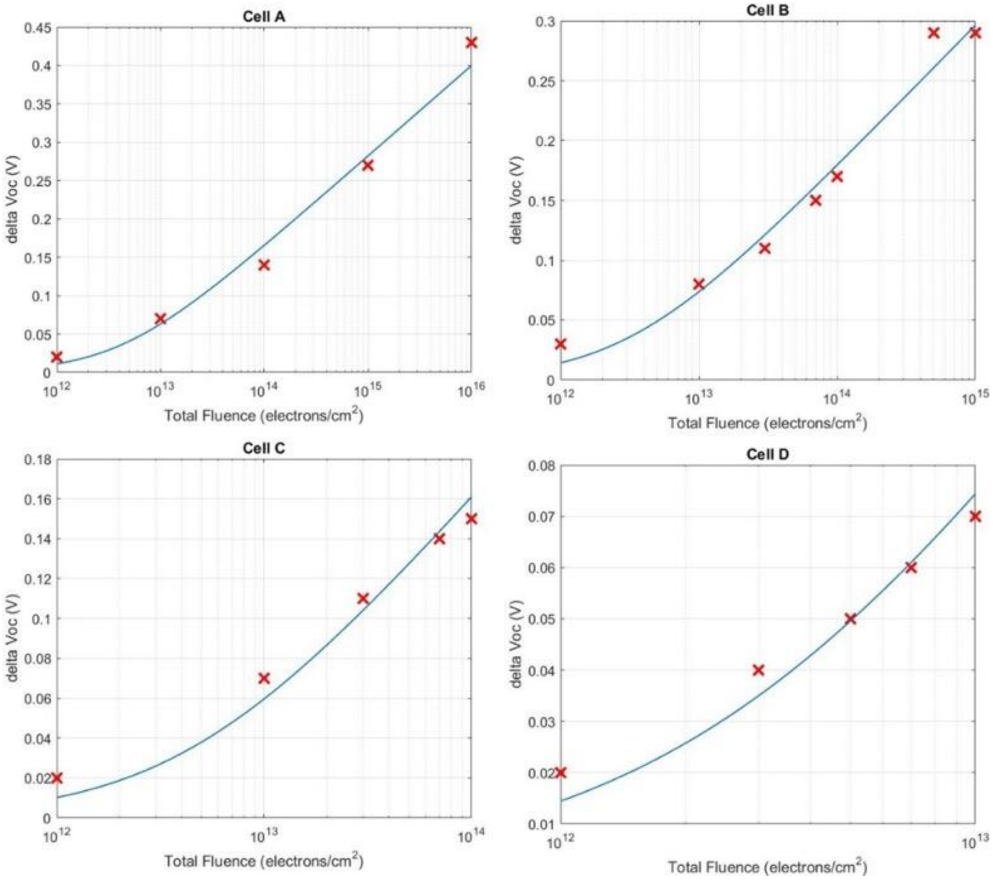

Figure 55. Delta V_{oc} as a Function of Total Fluence for all Cells with Non-Linear Regression Model Fitted

A comparison between the theoretical defect introduction rate using Equation 24 and the method in [31] using the measured drop in V_{oc} can now be made. Chen shows that the average displacement threshold energy is 13±1 eV for GaAs, but the maximum can be as high as 22 and 28 eV for gallium and arsenic, respectively [35]. The average value of 13.0 eV was used in determining the defect introduction rate using the SR-NIEL calculator. The results of the two methods are shown in Table 7.

Table 7. Defect Introduction Rates from NIEL Theory and Change in V_{oc}

Method	γ_R **[cm^{-1}]**
Theoretical using SR-NIEL	11.6
Calculated using change in V_{oc}	339.3

The results show a much larger rate of defects being created in the measured values vice the theoretical. The rate variation can possibly be accounted for in the assumption that the GaAs crystal measured in [34] contains the same concentration of native defects as the test devices irradiated. Additionally, the displacement threshold energy for GaAs can vary by a small amount, which changes the results for the theoretical values. In order to more thoroughly determine the rate of defect introduction, the concentration of native defects needs to be measured using a method such as DLTS.

VI. CONCLUSTION

The purpose of this thesis was to evaluate the radiation hardness of thin-film GaAs solar cells with applications to the space environment. The majority of the effort in doing this was spent developing robust test set-ups to characterize the devices. Once the baseline values for the cells were obtained, they were incrementally irradiated from 10^{12} cm^{-2} to 10^{16} cm^{-2}. The devices' illuminated DC IV characteristics were measured after each step in deposited radiation to gather a larger number of data points since there were only four devices from which to obtain data. The devices were exposed to 8.0 MeV electrons instead of the standard 1.0 MeV electrons as in most solar cell research. The total fluence for each device was halted at a different value so that EQE measurements could be taken at every decade from 10^{13} cm^{-2} to 10^{16} cm^{-2}. This allowed a thorough representation of performance versus fluence for such a small sample size.

The performance of the cells prior to irradiation was significantly worse than expected when compared to the published characteristics. The parameter that differed the most was short circuit current. This resulted in a much lower power conversion efficiency. Even though the absolute performance characteristics were degraded prior to irradiation, the relative change could still be used to evaluate the cells.

The test devices' IV characteristics showed a sharp decline in short circuit current after a fluence of 10^{13} cm^{-2}. The I_{sc} was less than 2% of its original value by 10^{16} cm^{-2}. Open circuit voltage did not suffer as significant a decline as I_{sc}; however, a reduction of over 40% occurred by a fluence of 10^{16} cm^{-2}. The maximum output power and power conversion efficiency followed a similar trend as I_{sc}.

The device EQE was reduced significantly over its entirety; however, by a fluence of 10^{16} cm^{-2} the only wavelengths of light that showed any device response were greater than 700 nm. The EQE results showed the region of majority damage was closer to the surface.

After irradiation, the change in V_{oc} was used to calculate a defect introduction rate and compare it to another method using the theoretical NIEL and the modified K-P model.

The rate of defects created in the test devices was nearly 30 times larger than estimated with the modified K-P model.

Based upon this research, the solar cells did not exhibit the performance post-irradiation necessary to consider their use in a space application.

A. FUTURE WORK

Preparing a system to perform DLTS measurements would allow the initial defect concentration to be determined. Additionally, the use of bare cells should be investigated in a similar fashion to this experiment in order to determine the effect of the plastic laminate, which would allow better imaging with a scanning electron microscope to determine layer thicknesses and composition. The very large drop-off in cell performance was much larger than initially expected, and further investigation into the construction of these cells and other thin-film technology is warranted.

APPENDIX. LABVIEW EQE VI

The VI used for measuring the test device EQE is shown in the Labview graphical programming block diagram format used. The VI front panel is shown in Figure 56 for reference. The shutter, measurement, and Background Iph buttons each have a separate associated block diagram shown in Figures 57 through 59, respectively. The EQE VI contains smaller embedded VIs named wavelength sweep and wavelength set shown in Figures 60 and 61, respectively.

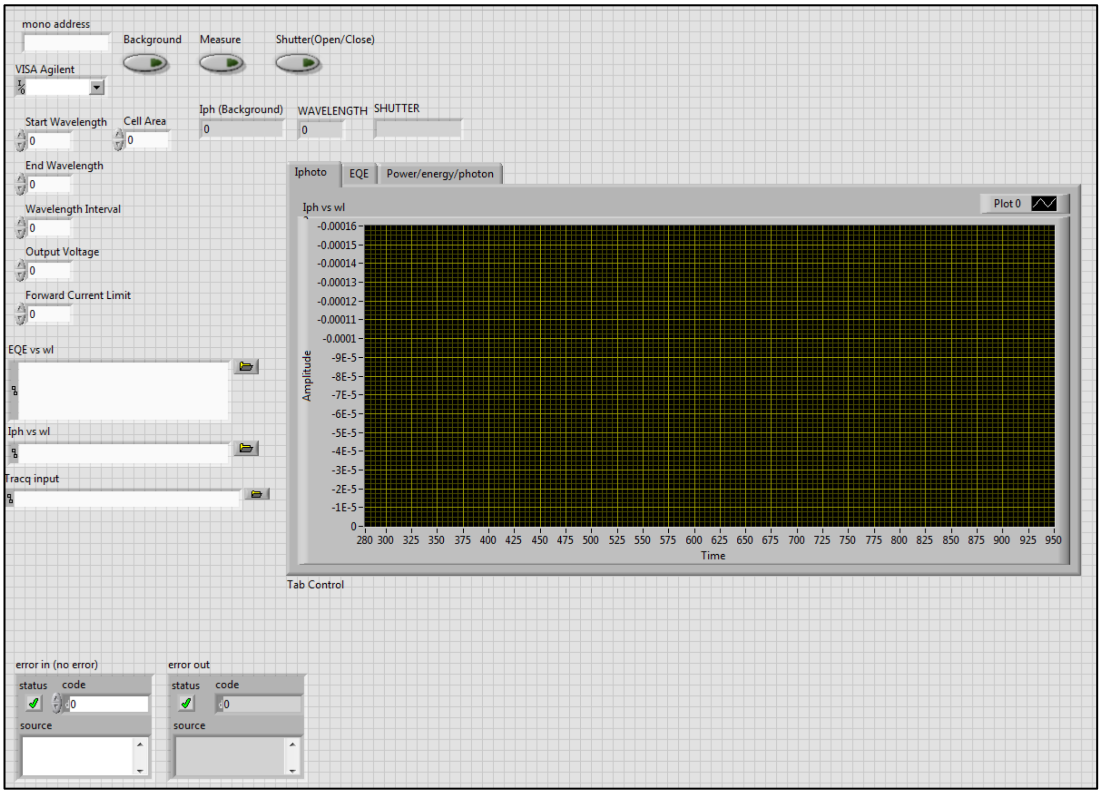

Figure 56. EQE VI Front Panel

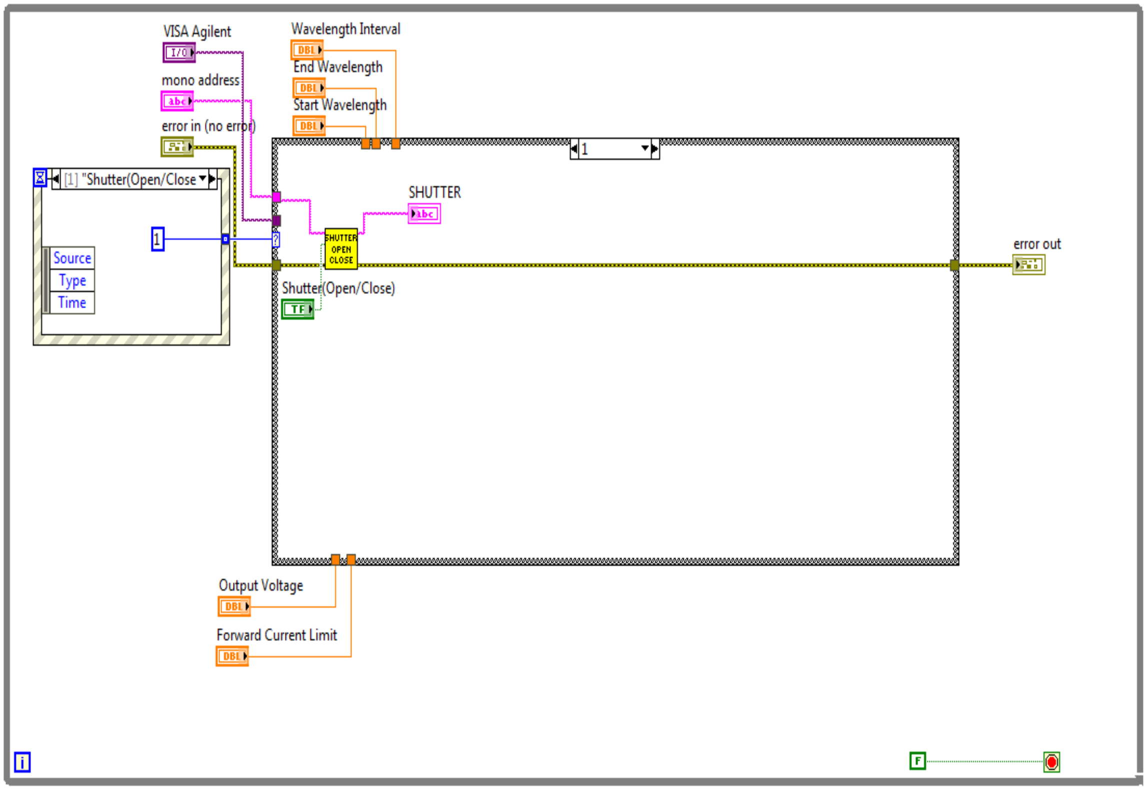

Figure 57. Shutter Button VI

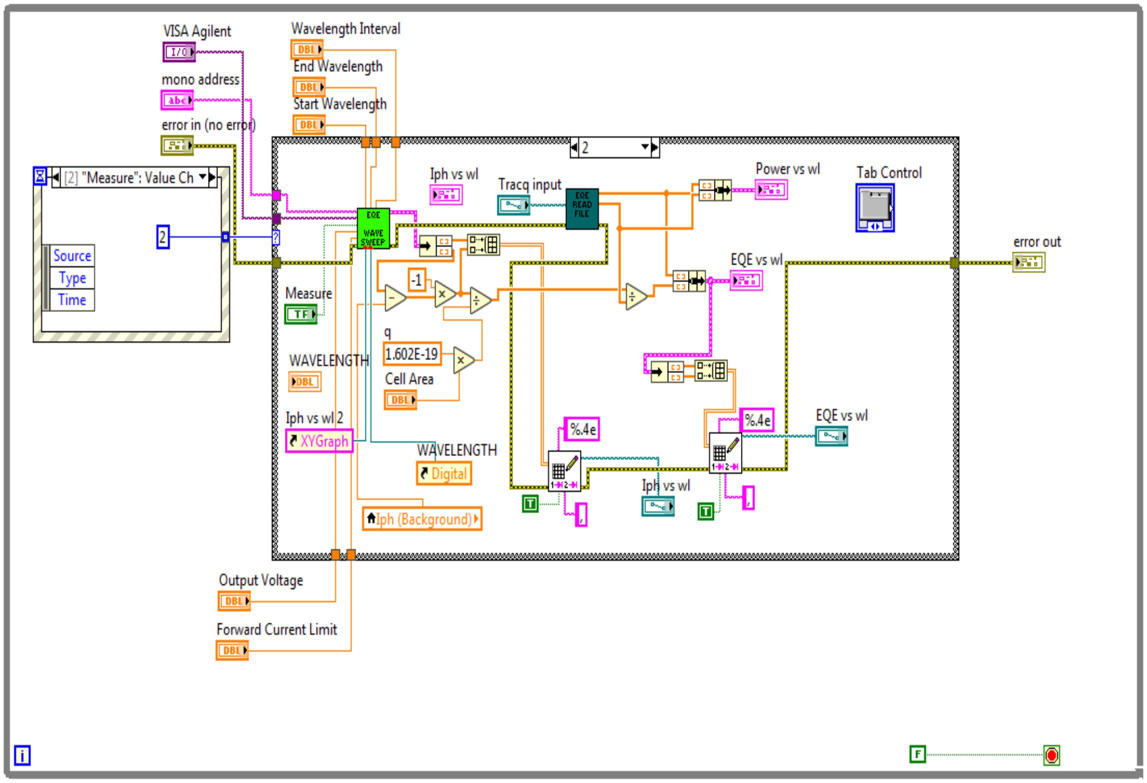

Figure 58. Measure Button VI

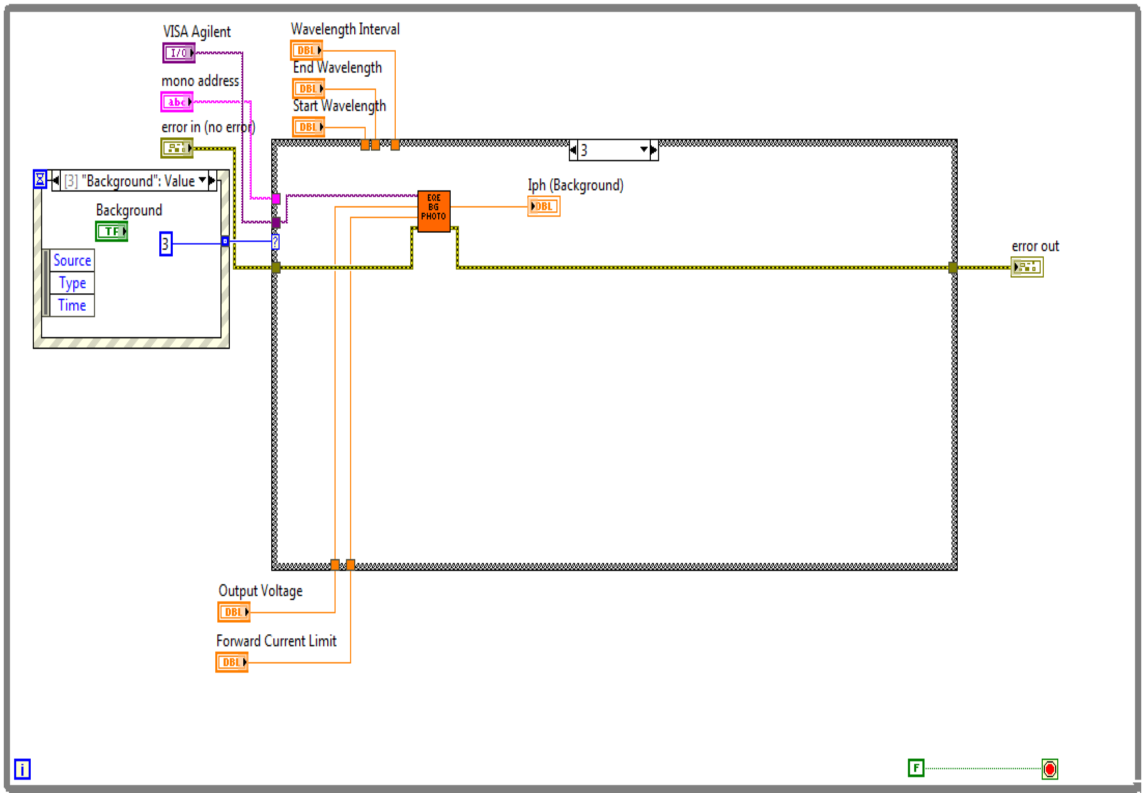

Figure 59. Background Iph Button VI

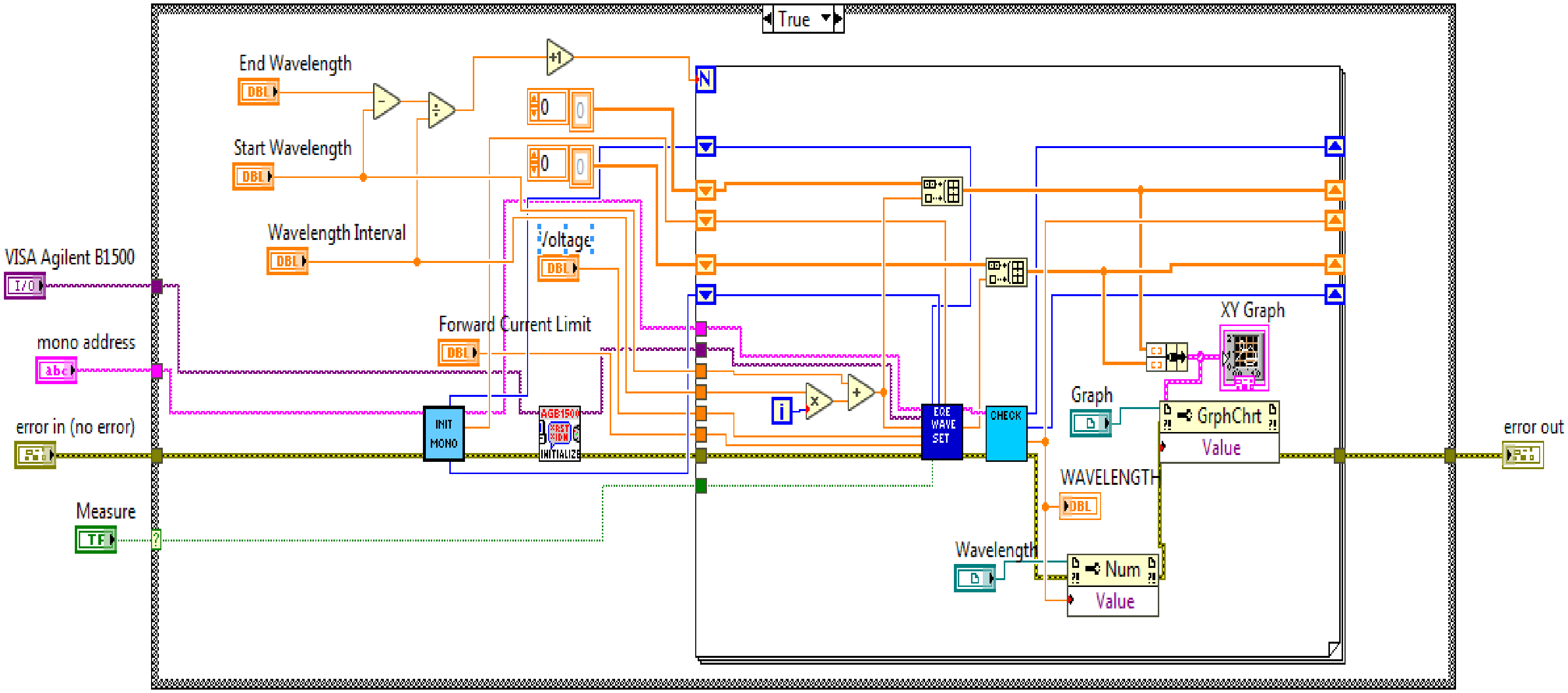

Figure 60. EQE Wavelength Sweep VI

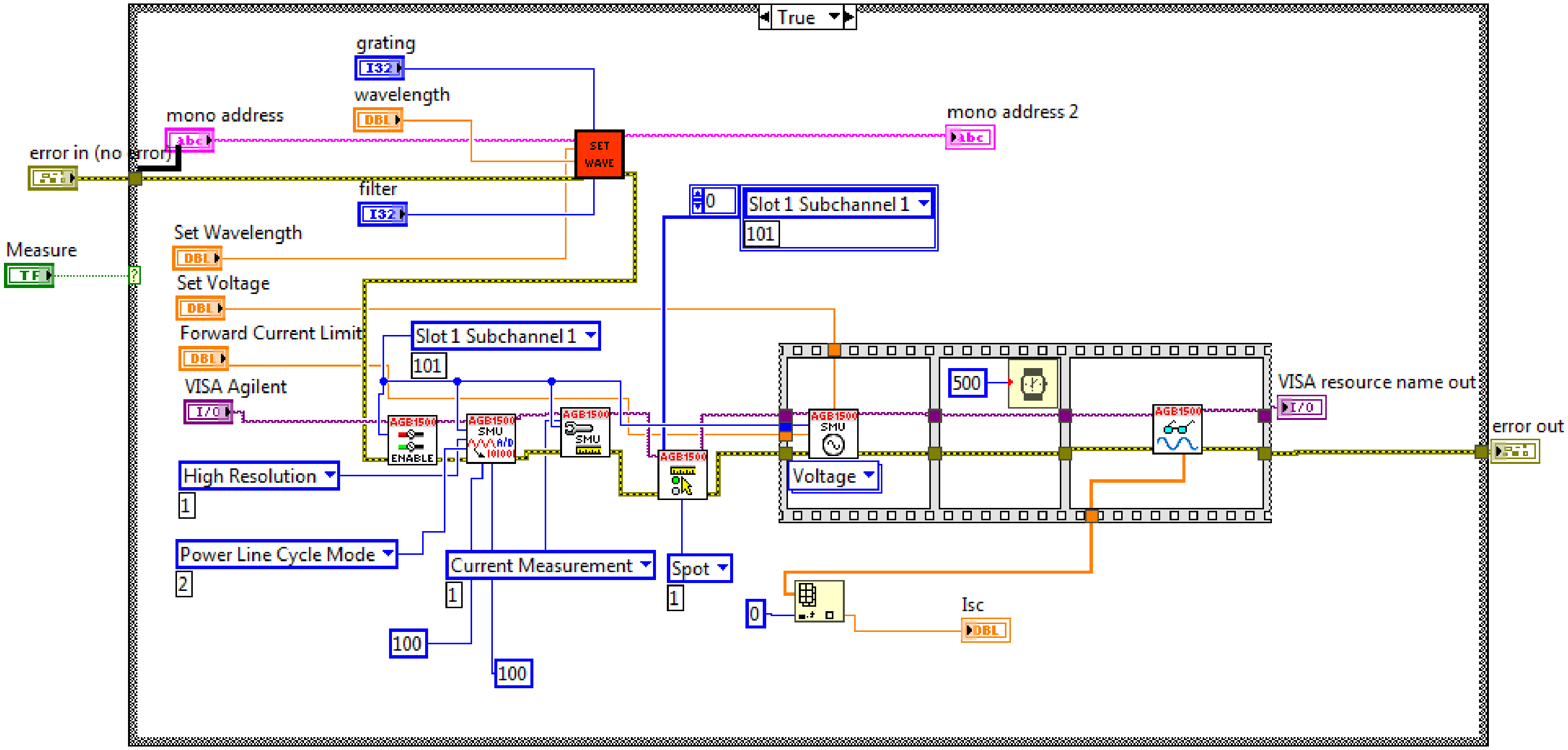

Figure 61. EQE Wavelength Set VI

LIST OF REFERENCES

[1] G.P. Smestad, *Optoelectronics of Solar Cells.* Bellingham, WA, USA: SPIE Press, 2002. [Online]. doi: 10.1117/3.446028

[2] M. O'Bryan, "The natural space radiation hazard," Radiation Effects and Analysis, November 15, 2000. [Online]. Available: https://radhome.gsfc.nasa.gov/radhome/Nat_Space_Rad_Haz.htm

[3] "Research cell record efficiency chart," National Renewable Energy Laboratory, Accessed April 25, 2018. [Online]. Available: https://www.nrel.gov/pv/assets/images/efficiency-chart.png

[4] "29.5% NeXt triple junction (XTJ) solar cells," Spectrolab, September 28, 2012. [Online]. Available: http://www.spectrolab.com/solarcells.htm

[5] D. Gold, "High energy electron radiation degradation of gallium arsenide solar cells," M.S. thesis, Dept. of Electrical and Comp. Engr., NPS, Monterey, CA, USA, 1986.

[6] T.L. Fifer, "Radiation effects on multi-junction solar cells," M.S. thesis, Dept. of Electrical and Comp. Engr., NPS, Monterey, CA, USA, 2001. [Online]. Available: http://handle.dtic.mil/100.2/ADA401081

[7] M.D. Woods, "A comparative analysis of radiation effects on silicon, gallium arsenide, and GaInP2/GaAs/Ge triple junction solar cells using a 30 MeV electron linear accelerator," M.S. thesis, Dept. of Electrical and Comp. Engr., NPS, Monterey, CA, USA, 2002. [Online]. Available: http://library.nps.navy.mil/uhtbin/hyperion/02Sep%5FWoods.pdf

[8] S.M. Sze and K.K. Ng, *Physics of Semiconductor Devices*, 3rd ed. Hoboken, NJ, USA: Wiley-Interscience, 2007.

[9] A. Johnston, *Reliability and Radiation Effects in Compound Semiconductors*. Hackensack, NJ, USA: World Scientific, 2010.

[10] "Solar Energy," class notes for Renewable Energy at Military Bases and for the Warfighter, Dept. of Electrical and Computer Engineering, Naval Postgraduate School, Monterey, CA, USA, spring 2017.

[11] C. Hu and R.M. White, *Solar Cells From Basics to Advanced Systems*. New York, NY, USA: McGraw-Hill, 1983. [Online]. Available: https://nanohub.org/resources/14073/download/Solar_cells_by_Hu_and_White_1.pdf

[12] D.K. Schroder, Semiconductor Material and Device Characterization, 3rd ed. Piscataway, NJ, USA: IEEE Press, 2006. [Online]. Wiley Online Library.

[13] A. Luque and S. Hegedus, Handbook of Photovoltaic Science and Engineering, 2nd ed. Chichester, West Sussex, UK: Wiley, 2011. [Online]. Knovel.

[14] C.R. Baraona, H.W. Brandhorst Jr., and M.P. Godlewski. "Effects of high doping levels silicon solar cell performance," NASA, TM-X-71728, 1975. [Online]. Available: https://ntrs.nasa.gov/archive/nasa/casi.ntrs.nasa.gov/19750016045.pdf

[15] P. Nubile, "Bandgap narrowing effects on the open circuit voltage in Si, GaAs and InP solar cells," *Solid State Electron.*, vol. 38, no.1, 1995. [Online]. Available: https://torpedo.nrl.navy.mil.libproxy.nps.edu/tu/ps/doc.html?vol=38&dsn=46924&ssn=190&iss=1&st=JRNAL

[16] R.E. Hart Jr., C.K. Swartz, I. Weinberg, and R.L. Statler. "Radiation and temperature effects in gallium arsenide, indium phosphide and silicon solar cells," NASA, TM-89870, 1987. [Online]. Available: https://ntrs.nasa.gov/search.jsp?R=19870012665

[17] K. Lee, "Compound semiconductor-based thin-film and flexible optoelectronics," Ph.D. dissertation, Dept. of Elec. Eng. and Comput. Sci., Univ. of Michigan, Ann Arbor, MI, USA, 2015. [Online]. Available: https://babel.hathitrust.org/cgi/pt?id=mdp.39015089717477

[18] D.C. Law, J.C. Boisvert, E.M. Rehder, P.T. Chiu, S. Mesropian, R.L. Woo, X.Q. Liu, W.D. Hong, C.M. Fetzer, S.B. Singer, D.M. Bhusari, K.M. Edmondson, A. Zakaria, B. Jun, D.D. Krut, R.R. King, S.K. Sharma, and N. H. Karam, "Recent progress of Spectrolab high-efficiency space solar cells," in *Proc. of the 38th IEEE Photovoltaic Specialists Conf.*, 2012. [Online]. doi: 10.1109/PVSC.2012.6318246

[19] "How Alta works," Alta Devices, December 27, 2012. [Online]. Available: https://www.altadevices.com/resources/

[20] J.J. Schermer, P. Mulder, G.J. Bauhuis, P.K. Larsen, G. Oomen, and E. Bongers, "Thin-film GaAs epitaxial lift-off solar cells for space applications," *Progress in Photovoltaics: Res. and Applications*, vol. 13, no. 7, pp. 587-596, Nov. 2005. [Online]. Doi:10.1002/pip.616

[21] J. Becker, Y. Kuo, and Y. Zhang, "Increased radiation hardness in ultra-thin GaAs single-junction solar cells," in *Proc. of the 40th IEEE Photovoltaic Specialist Conf.*, 2014. [Online]. doi: 10.1109/PVSC.2014.6925281

[22] L.M. Fraas and L.D. Partain, *Solar Cells and Their Applications*. Hoboken, NJ, USA: Wiley, 2010. [Online]. Available: https://ebookcentral.proquest.com/lib/ebook-nps/detail.action?docID=564956

[23] "Describing orbits," class notes for Space Technology and Applications, Dept. of Space Syst., Naval Postgraduate School, Monterey, CA, USA, summer 2017.

[24] M. Soria-Santacruz, H.B. Garrett, R.W. Evans, I. Jun, W. Kim, C. Paranicas, and A. Drozdov, "An empirical model of the high-energy electron environment at Jupiter," *Journal of Geophysical Research: Space Physics*, vol. 121, no. 10, pp. 9732-9743, October 2016. [Online]. doi: 10.1002/2016JA023059

[25] D.R. Williams, "Jupiter fact sheet," NASA, June 30, 2017. [Online]. Available: https://nssdc.gsfc.nasa.gov/planetary/factsheet/jupiterfact.html

[26] T.L. Cline and F.B. McDonald. "Relativistic electrons from solar flares," NASA Goddard Space Flight Center, Greenbelt, MD, USA, NASA TM-X-63210, 1968. [Online]. Available: https://ntrs.nasa.gov/archive/nasa/casi.ntrs.nasa.gov/19680015255.pdf

[27] V.A.J. van Lint, R.E. Leadon, J.F. Colwell, "Energy dependence of displacement effects in semiconductors," *IEEE Trans. On Nucl. Sci*., vol. 19, no. 6, pp. 181-185, Dec. 1972. [Online]. doi: 10.1109/TNS.1972.4326830

[28] G. S. Was, *Fundamentals of Radiation Materials Science Metals and Alloys.* New York, NY, USA: Springer-Verlag, 2007. [Online]. 10.1007/978-1-4939-3438-6

[29] M.J. Boschini, P.G. Rancoita, and M. Tacconi, "SR-NIEL Calculator: Screened Relativistic (SR) Treatment for Calculating the Displacement Damage and Nuclear Stopping Powers for Electrons, Protons, Light- and Heavy- Ions in Materials (version 3.9.5)," SR-NIEL, February 2018. [Online]. Available: http://www.sr-niel.org/

[30] M.A. Alam, "Non-ideal effects," class notes for ECE606: Solid State Devices, Dept. of Elec. and Comp. Engr., Purdue University, West Lafayette, IN, USA, spring 2009. [Online]. Available: https://nanohub.org/resources/5824

[31] A. Jasenek and U. Rau, "Defect generation in Cu(In,Ga)Se$_2$ heterojunction solar cells by high-energy electron and proton irradiation," *J. of Appl. Physics*, vol. 90, no. 2, pp. 650-658, Jul. 2001. [Online]. doi: 10.1063/1.1379348

[32] ASTM E-490, Standard Solar Constant and Zero Air Mass Solar Spectral Irradiance Tables, 2014. [Online]. Available: https://www.pveducation.org/pvcdrom/appendices/standard-solar-spectra

[33] Alta Devices, *Technology brief-single junction (preliminary),* TB-SJC-1804-001-EN, 2018. [Online]. Available: https://www.altadevices.com/wp-content/uploads/2018/04/Single-Junction-Tech-Brief.pdf

[34] M.O. Watanabe, A. Tanaka, T. Nakansi, and Y. Zohta, “Effects of growth conditions on deep level concentration in MOCVD GaAs,” *Japanese J. of Appl. Physics*, vol. 20, no. 6, pp. L429-L432, Jun. 1981. [Online]. doi: 10.1143/JJAP.20.L429

[35] N. Chen, S. Gray, E. Hernandez-Rivera, D. Huang, P.D. LeVan, and F. Gao, “Computational simulation of threshold displacement energies of GaAs,” *J. of Materials Res.*, vol. 32, no. 8, pp. 1555-1562, Feb. 2017. [Online]. doi: 10.1557/jmr.2017.46

INITIAL DISTRIBUTION LIST

1. Defense Technical Information Center
   Ft. Belvoir, Virginia

2. Dudley Knox Library
   Naval Postgraduate School
   Monterey, California